An atlas of inter- and intra-tumor heterogeneity of apoptosis competency in colorectal cancer tissue at single cell resolution

Andreas Ulrich Lindner[1,2], Manuela Salvucci[1,2], Elizabeth McDonough[3], Sanghee Cho[3], Xanthi Stachtea[4], Emer Patsy O'Connell[1,2,5], Alex D Corwin[3], Alberto Santamaria-Pang[3], Steven Carberry[1,2], Michael Fichtner[1,2], Sandra Van Schaeybroeck[4], Pierre Laurent-Puig[6], John P Burke[5], Deborah A McNamara[5,7], Mark Lawler[4], Anup Soop[3], John F Graf[3], Markus Rehm[8], Philip Dunne[4], Daniel B Longley[4], Fiona Ginty[3], Jochen HM Prehn*[1,2]

[1]Department of Physiology and Medical Physics; [2]Centre of Systems Medicine; [5]Department of Surgery, Royal College of Surgeons in Ireland University of Medicine and Health Sciences, 123 St. Stephen's Green, Dublin 2, Ireland.
[3]GE Research, Niskayuna, NY 12309, USA.
[4]Centre for Cancer Research & Cell Biology, Queen's University Belfast, 97 Lisburn Road, Belfast, BT9 7AE, Northern Ireland, UK.
[6]Centre de Recherche des Cordeliers, INSERM, CNRS, Université de Paris, Sorbonne Université, USPC, Equipe labellisée Ligue Nationale Contre le Cancer, Paris, France.
[7]Beaumont Hospital, Beaumont Road, Dublin 9, Ireland
[8]Institute of Cell Biology and Immunology, University of Stuttgart, Allmandring 31, 70569 Stuttgart, Germany.

***Corresponding Author:** Jochen HM Prehn, Department of Physiology and Medical Physics, Royal College of Surgeons in Ireland, 123 St. Stephen's Green, Dublin 2, Ireland; prehn@rcsi.ie.

Abstract

Cancer cells' ability to inhibit apoptosis is key to malignant transformation and limits response to therapy. Here, we performed multiplexed immunofluorescence analysis on tissue microarrays with 373 cores from 168 patients, segmentation of 2.4 million individual cells and quantification of 20 cell lineage and apoptosis proteins. Ordinary differential equation-based modelling of apoptosis sensitivity at single cell resolution was conducted and an atlas of inter- and intra-tumor heterogeneity in apoptosis susceptibility generated. We identified an enrichment for BCL2 in immune, and BAK, SMAC and XIAP in cancer cells. ODE-based modelling at single cell resolution identified an enhanced sensitivity of cancer cells to mitochondrial permeabilization and executioner caspase activation compared to immune and stromal cells, with significant inter- and intra-tumor heterogeneity. However, we did not find increased spatial heterogeneity of apoptosis signaling in cancer cells, suggesting that such heterogeneity is an intrinsic, non-genomic property not increased by the process of malignant transformation.

Introduction

Alterations in apoptosis signaling is key step in tumorigenesis(Hanahan and Weinberg, 2011). In many cases, cancer epithelial cells over time acquire alterations in their genome or epigenome that either result in an up-regulation of anti-apoptotic or a down regulation of pro-apoptotic proteins. Examples for such (epi)genomic alterations include promoter methylation and copy number alterations (Berdasco and Esteller, 2010; Mauro et al., 2015), while single point mutations in apoptosis-regulating genes are relatively rarely observed. Previous quantitative studies in solid tumor tissues found significant, but often complex differences in levels of individual anti- or pro-apoptotic proteins between different patients (Lindner et al., 2013; Lindner et al., 2017; Salvucci et al., 2017; Salvucci et al., 2019b). Predictions of individual patient's apoptosis susceptibility is further complicated by the signaling redundancies in key apoptosis pathways, in particular the mitochondrial apoptosis pathway. Here, activation of either BAK or BAX is sufficient to induce mitochondrial outer membrane permeabilization (MOMP) (Kalkavan and Green, 2018), and this process is inhibited by a variety of different anti-apoptotic Bcl-2 family proteins including BCL2 itself, BCL(X)L and MCL1(Certo et al., 2006; Kalkavan and Green, 2018). Research into Bcl-2 family proteins and other apoptosis signaling proteins have resulted in the development and subsequent clinical approval of apoptosis sensitizers as anti-cancer agents. For example, Venetoclax is a selective BCL2 antagonist now used for the treatment of chronic lymphocytic leukemia, small lymphocytic lymphoma and acute myeloid leukemia which are characterized by strong BCL2 overexpression and dependency (Roberts et al., 2016). In context of solid tumors, the entry of apoptosis sensitizers into clinical practice has been relatively slow, a fact that is partially explained by the lack of gene mutations or pronounced over- or under-expression of individual apoptosis signaling proteins in solid tumor cells which could otherwise serve as stratification tools in clinical trials.

To overcome such limitations, various groups have developed computational models that describe apoptosis sensitivity on a systems level. BH3-only proteins are upstream initiators of the mitochondrial apoptosis pathway that are activated transcriptionally or post-translationally in response to stresses, such as DNA damage, genotoxic drugs, irradiation or withdrawal of trophic support. BH3-only proteins activate BAK and BAX directly, or activate these indirectly by binding to and neutralizing anti-apoptotic Bcl-2 proteins (Leber et al., 2007). BH3-peptide profiling has been successfully applied to predict outcome and responses to cancer therapeutics in solid cancers, however this technique requires fresh tissue (Ni Chonghaile et al., 2011). Other groups, including our own, have used gene expression or protein level (Reverse Protein Phase Array, RPPA) data of apoptosis-regulating genes from fresh-

68 frozen or formalin-fixed tissues as input into deterministic signaling network models to estimate the
69 intrinsic apoptosis sensitivity of individual tumors (Lindner et al., 2017; Salvucci et al., 2017).

70 Notwithstanding the successful application of these techniques in predicting chemotherapy responses
71 and clinical outcome in cancer patients, the above techniques usually require a tissue homogenate to
72 be analyzed. However, such "bulk" profiling results in the loss of not only important spatial
73 information but also the precise cell-of-origin of the signals. It is feasible that some cancer cell
74 populations in a given tumor are more resistant to therapy than other cancer cells, which is in line
75 with evidence indicating the role of tumor heterogeneity in determining clinical outcome and
76 responses to therapy (Fisher et al., 2013; Marusyk et al., 2012). Such resistant cell populations could
77 give rise to more aggressive tumors on recurrence. Similarly, chemo- or radiation therapy not only
78 affects tumor cells, but also cells in the tumor microenvironment such as immune cells; therefore, a
79 higher apoptosis sensitivity of anti-tumor immune cells compared to cancer epithelial cells may be
80 detrimental to patients.

81 To describe the extent of inter-individual and intra-tumor heterogeneity in apoptosis signaling, herein
82 we employed an innovative multiplexed immunofluorescence imaging technique (Cell DIVE™), which
83 is comprised of a repeated stain-image-dye-inactivation sequence using direct antibody-fluorophore
84 conjugates, as well as a small number of primary antibodies from distinct species with secondary
85 antibody detection (Gerdes et al., 2013), followed by single cell segmentation in a colorectal tumor
86 tissue cohort. Using this method, we imaged 20 proteins and mapped quantities of the key members
87 of the mitochondrial apoptosis pathway to 2.4 million individual cells (of which 1.6 million were
88 colorectal tumor epithelial cells). This enabled us to calculate each individual cell's apoptosis
89 sensitivity through single cell systems modelling, and quantitatively describe inter- and intra-tumor
90 heterogeneity of the mitochondrial apoptosis pathway within the different cell types that constitute
91 a colorectal tumor.

92 To assess intrinsic apoptosis sensitivity of individual tumors, we had previously applied *'averaged'*
93 protein levels of tissue, but never single cell levels to our experimentally validated models, APOPTO-
94 CELL (Huber et al., 2007; Rehm et al., 2006) and DR_MOMP (Lindner et al., 2013). Studying single cells'
95 with our apoptosis models is providing us with new insights into the mechanisms underlying apoptosis
96 and treatment resistance.

Results

Multiplexed immunofluorescence imaging generates single cell profiles of mitochondrial apoptosis pathway proteins in 1.6 million individual colorectal tumor cells

To explore the levels of key proteins of the mitochondrial apoptosis pathways in colorectal cancer (CRC) tissue at the single cell level, we performed Cell DIVE™ multiplexing of nine pro- and anti-apoptotic proteins in regions of resected primary tumors in 355 tumor cores derived from 164 stage III CRC patients.

Apoptosis signaling protein selected for analysis included BCL2, BCL(X)L, MCL1, BAK and BAX which regulate the process of mitochondrial outer membrane permeabilization (MOMP), as well as PRO-CASPASE 9, PRO-CASPASE 3, XIAP and SMAC (DIABLO) which control the process of executioner caspase activation downstream of MOMP. For both processes, we previously devised and experimentally validated ordinary differential equation (ODE)-based, deterministic models, APOPTO-CELL (Huber et al., 2007; Rehm et al., 2006) and DR_MOMP (Lindner et al., 2013), that calculate the sensitivity of cancer cells to undergo mitochondrial apoptosis with high accuracy (Lindner et al., 2017; Salvucci et al., 2017), using quantities of the above 9 proteins as model input. Additional proteins selected for this study included cell identity markers (CD3, CD4, CD8, CD45, FOXP3, PCK26 and cytokeratin AE1), established markers of cell proliferation (KI67), antigen-presenting protein (HLA-A) and bioenergetics (GLUT1, CA9), as well as proteins used for cell segmentation analysis (Na+/K+-ATPase, cytokeratin AE1, PCK26, and S6).

We proceeded with multiplexed data acquisition of colon tumor tissue as follows (Figure 1A): 1-5) FFPE cores where formalin fixed paraffin embedded (FFPE) tissue microarrays first underwent antigen retrieval, followed by repeated cycles of protein staining, imaging and dye inactivation using cyanine dyes (Cy3 and Cy5) conjugated antibodies. DAPI staining and a background image was acquired in the beginning of each cycle for quality control and image processing. After rudimentary image processing (including illumination correction, distortion, stitching and registration) 6) we performed cell segmentation and single cell densitometry analysis. 7) We assessed the image quality of each core and removed 48 cores with insufficient quality. 8) We corrected possible batch effects between the five slides applying affine matrix transformations using an averaged distribution of protein intensities as reference for each protein marker. 9) Finally, we performed core and single cell analysis of the markers and performed model calculations within different cell populations.

128 This delivered a total of 54.6 million protein profiles (Figure 1B) in a total of 2.4 million cells which
129 were used for cell identity analysis, construction of a tissue atlas of apoptotic proteins profiles, intra-
130 and inter-tumor heterogeneity analysis, spatial tissue analysis as well as single cell systems modelling.

131 Cell DIVE™ and cell segmentation analysis identified on average 6,492 (SD 1,228) cells per tissue
132 microarray (TMA) core; totaling on average 14,414 (SD 4,196) cells per patient (1 to 3 cores; Figure
133 1B). Cells were classified into different cell types based on cell identity markers for cancer/epithelial
134 cells (positive for cytokeratin AE1 or PCK26), immune cells (positive for CD3, CD4, CD8 or CD45) and
135 other stromal cells that were negative for any of these markers. For more extensive cell classification,
136 a Random Forest model was trained with 15,184 manual annotated cells (0.6% of total cells) and CD3,
137 CD4, CD8, CD45 and FOXP3, and applied on 99.9% of all cells to further differentiate immune cells into
138 Cytotoxic, Regulatory, Helper T and other immune cells (Figure 1C). The model classified 65.7% as
139 (epithelial like) cancer cells (type II error 3.0%; training set), 23.6% other stromal cells (type II error
140 8.1%) and 10.7% as immune cells (type II error 3.0%), of which 2.0% were Helper (type II error 28.8%),
141 1.4% Regulatory (type II error 7.4%), 1.3% Cytotoxic (type II error 28.0%) and 6.0% other T or immune
142 cells (type II error 18.8%; Figure 1DE). Of note, the cell type composition in CRC core tissues varied
143 significantly, with some cores showing predominantly cancerous/epithelial cells in the absence of
144 immune cell infiltration, and others showing very high levels (up to 55%) of immune cells (Figure 1D).
145 The median distribution of cells was 66.5% tumor, 7.8% immune and 22.2% stromal cells (Figure 1E).
146 A bootstrap analysis with sampled pairings suggested that cell type composition in tumors of patients
147 with paired-cores were, despite high heterogeneity, more similar to each other compared to random
148 pairings. This suggests that cell type composition was a biological feature of individual tumors (Suppl.
149 Figure 1).

150 Tumor cell atlas shows heterogeneous and cell-type specific 151 enrichment of key proteins of the mitochondrial apoptosis pathway

152 We next calculated molar protein profiles for proteins that are key to control MOMP and are used as
153 input for the deterministic systems model, DR_MOMP. For the calculations of protein profiles of
154 individual cells, we normalized cell intensities to the mean intensity in HeLa cells and used previously
155 established concentrations in HeLa cells as reference (Flanagan et al., 2015; Lindner et al., 2013).

156 Analysis of the five key BCL2 proteins that control the process of MOMP demonstrated a significant
157 enrichment in anti-apoptotic BCL2 in immune cells when compared to cancerous epithelial cells or
158 other stromal cells, while anti-apoptotic BCL(X)L and MCL1 although statistically enriched in cancer
159 epithelial cells were more homogenously distributed between the three cell types (Figure 2A-C). Mean

160 levels of MCL1 were in general lower compared to BCL2 and BCL(X)L, confirming previous studies
161 (Lindner et al., 2013). Of note, pro-apoptotic BAK showed a strong enrichment in cancer cells
162 (Figure 2A-C), while again BAX, although statistically enriched in cancer cells, was more homogenously
163 distributed between the three cell types.

164 For PRO-CASPASE 3, PRO-CASPASE 9, SMAC and XIAP single protein profiling we converted the batch-
165 corrected protein intensities to µM concentrations via alignment with reference distributions (Hector
166 et al., 2012) using a pipeline that we previously developed (Salvucci et al., 2019a; Salvucci et al., 2017).
167 Proteins that control executioner caspase activation downstream of MOMP also showed a
168 heterogeneous distribution between cell types, with XIAP, SMAC, PRO-CASPASE 3 and PRO-
169 CASPASE 9, all at higher levels in cancer cells when compared to immune cells (Figure 2D-F). Stromal
170 cells showed the lowest levels of these proteins, suggesting that the apoptotic machinery downstream
171 of MOMP is suppressed in non-transformed cells when compared to cancer epithelial cells.

172 Utilizing transcriptional data derived from flow-sorted immune ($n = 6$), epithelial ($n = 6$) and fibroblast
173 ($n = 6$) populations isolated from CRC primary tumor tissue (GSE39396 (Calon et al., 2012); Suppl.
174 Table 2), we identified elevated levels of *bcl2* mRNA levels in leukocytes compared to cancer
175 (epithelial) cells (ANOVA $p = 0.006$, Tukey post-hoc $p = 0.005$) but also significantly higher levels of bax
176 and mcl1 mRNA levels in Leukocytes compared to cancer cells, and in Stroma (Fibroblasts) compared
177 to cancer cells (ANOVA $p \leq 0.01$, Tukey post-hoc $p < 0.01$; Suppl. Figure 2). We did not find any
178 significant differences in mRNA levels of the *bak1*, *bcl2l1* (BCL(X)L), caspases, nor *xiap* between the
179 cell populations.

180 Apoptotic protein profiles from approximate 115,923 identified T cells showed higher levels of BAK,
181 XIAP, SMAC, PRO-CASPASE 3 and PRO-CASPASE 9 and lower levels of BCL2 in Cytotoxic T cells when
182 compared to Helper or Regulatory T cells (Figure 3A-C). These findings suggests that Cytotoxic T cells
183 may represent the T cells most sensitive to the activation of mitochondrial apoptosis.

184 As expected, cancer epithelial cells also showed higher levels of the glucose transporter GLUT1,
185 sodium-potassium ATPase, the hypoxia-inducible factor-1α (HIF-1a) target gene CA9, and the
186 proliferation marker KI67, while HLA-A were enriched in immune cells (Figure 4AB). In contrast,
187 protein levels of p70S6 kinase (S6) were more evenly distributed across all cell types. Calculating the
188 cores' quartile coefficients of dispersion (COD; Suppl. Figure 3), a measure of the spread of the protein
189 levels, we found that immune cells had a greater COD for BCL2 and BAK compared to cancer and
190 stroma cells. Stroma cells showed the highest, and cancer epithelial cells the lowest, COD for MCL1,

191 APAF1 and PRO-CASPASE 3. Cancer cells showed greater CODs of SMAC, GLUT1 and KI67 protein levels
192 compared to immune and stroma cells.

193 Correlation analysis (Figure 4C-D) of the 1,556,581 cancer cells demonstrated high, positive median
194 Spearman's correlation coefficients (ρ > 0.5) between BAK and BAX levels. Levels between BAK (and
195 BAX) and PRO-CASPASE 3 (and PRO-CASPASE 9), BCL(X)L and BCL2, PRO-CASPASE 3 and BCL2, BCL2
196 and MCL1, BCL2 and XIAP, SMAC and BCL(X)L, PRO-CASPASE 3 and PRO-CAPSASE 9, and PRO-
197 CASPASE 3 and XIAP had high positive median correlation coefficients in cancer and stromal, but not
198 immune cells. The Spearman's correlation coefficient between BCL(X)L and MCL1, CA9 and XIAP, and
199 SMAC and XIAP levels was > 0.5 in all cells. Comparing GLUT1 to apoptosis protein levels returned
200 coefficients around 0, but showed greater values when compared to HLA-A and CA9 in cancer cells.
201 HLA-A levels correlated with PRO-CASPASE 3 levels only in stromal cells. Generally, correlations
202 between individual proteins were nearly identical in leukocytes and stromal cells and frequently
203 differed from those in cancer cells, validating at the single cell level that transformed cells deviate
204 from a physiological regulation of apoptotic and metabolic pathways.

205 Single cell systems modelling of apoptosis sensitivity shows inter-
206 individual differences in apoptosis sensitivity and an enhanced
207 ability of tumor cells to undergo Caspase-3-dependent
208 mitochondrial apoptosis

209 Next, we used quantitative single cell protein profiles to predict the apoptosis sensitivity of the
210 1.6 million colorectal tumor cells. We employed two systems models of the mitochondrial apoptosis
211 pathway that were previously established and experimentally validated in our group to predict the
212 intrinsic ability of cells to initiate and execute apoptosis. DR_MOMP (Flanagan et al., 2015; Lindner et
213 al., 2013; Lindner et al., 2017) calculates the sensitivity of cells to undergo mitochondrial
214 permeabilization by computing a score that, in summary, quantifies the amount of pro-apoptotic BH3-
215 only proteins required to trigger sufficient BAK or BAX pore formation to induce mitochondrial outer
216 membrane permeabilization (MOMP) during genotoxic stress (Figure 5A). In contrast, APOPTO-CELL
217 (Huber et al., 2007; Rehm et al., 2006) calculates the amount of caspase 3 mediated substrate cleavage
218 as a consequence of MOMP and apoptosome formation (Figure 5A).

219 Using the quantitative Bcl-2 protein profiles of BAK, BAX, BCL2, BCL(X)L and MCL1 as model input for
220 DR_MOMP, we were able to calculate the sensitivity of individual tumor cells to the process of
221 mitochondrial apoptosis initiation. Calculating mean DR_MOMP scores for each core (Figure 5B, top)
222 and % cells with low sensitivity for MOMP for individual core (Figure 5B, bottom) using the calculated

223 average stress dose of the population as threshold (Flanagan et al., 2015; Lindner et al., 2013; Lindner
224 et al., 2017), we were able to show significant differences in % cells with low sensitivity for MOMP in
225 this otherwise homogeneous cohort of stage III CRC patients. Between patient-matched cores, we
226 found a mean difference of 18.8% ± SD 14.1% and a mean SD of 14.0% cells with low sensitivity for
227 MOMP. When stratifying DR_MOMP calculations for individual cell types, we found that, on average,
228 significantly fewer cancer cells and stromal cells exhibited low sensitivity for MOMP when compared
229 to immune cells (Figure 5C, upper). Among immune cells, Regulatory T cells were found to have largest
230 population of single cells with low sensitivity for MOMP (Figure 5C lower). And, in line with our analysis
231 on protein level (Figure 3), we found that cytotoxic T cells are overall significantly more susceptible to
232 apoptosis stimuli compared to other immune cells. Figure 5D depicts examples of DR_MOMP
233 predictions in cores with a majority of cells having a high sensitivity for MOMP (left) or a majority of
234 cells having low sensitivity for MOMP (right).

235 When investigating the sensitivity of individual tumor cells to undergo caspase 3 activation (once the
236 process of MOMP is activated) using the APOPTO-CELL systems model, we similarly found significant
237 differences between individual patients (Figure 5E, top) and cores (Figure 5E, bottom): Between
238 patient-matched cores we found a mean difference of 18.8% ± SD 15.7% and a mean SD of 13.8% cells
239 with low predicted caspase activity. Importantly, when investigating individual cell types, we found
240 that cancer cells were predicted to show a higher caspase activity compared to immune cells and
241 stromal cells, with the latter showing the greatest fraction of cells with low predicted caspase activity
242 (Figure 5F). Figure 5G depicts examples of cores with APOPTO-CELL predicting the majority of cells
243 showing high caspase activity (left) or the majority of cells exhibiting low caspase activity (right).

244 The activation of mitochondrial (or intrinsic) apoptosis is considered to be a two-step process, with
245 little feed-back from one to the other process (Ichim and Tait, 2016). The multiplexing, quantitative
246 protein profiling and single cell systems modelling pipeline developed here hence also allowed us to
247 address the question of whether cancer cells show differences in their ability to activate each of these
248 two apoptotic control points.

249 In line with the latter analysis, assessing apoptosis sensitivity up- and downstream of MOMP showed
250 that cancer cells are sensitive for both apoptosis pathways in the majority of tumors and that only a
251 small fraction of cores showed low sensitivity in both pathways at the same time (Figure 6A). In
252 contrast, immune and stroma cells had a higher fraction of cells that showed low sensitivity in both
253 pathways, and a lower fraction of cells that showed high sensitivity in both, compared to cancer cells
254 (Figure 6AB). Of the cancer of cells that show low sensitivity in one and high sensitivity in the other
255 pathway, we found that a majority of cancer cells showed a low MOMP sensitivity and a predicted

256 high caspase activity (Figure 6A-C). In contrast, the majority of immune cells showed a predicted high
257 caspase activity but a low sensitivity for MOMP (Figure 6A-C), and the majority of stroma cells showed
258 a high sensitivity for MOMP but a predicted low caspase activity (Figure 6A-C). Collectively, the data
259 suggested that the majority of cancer cells showed a high sensitivity for at least one of the two
260 apoptosis pathways, and that cancer cells were overall more likely to respond to both signaling
261 pathways when compared to immune or stromal cells.

262 Analysis of intra-tumoral heterogeneity

263 While investigating apoptosis sensitivity at the single cell level using our systems models, we also
264 noticed that certain patients showed a significant intra-tumor heterogeneity among cancer cells, while
265 other patients showed a more homogenous distribution in model predictions (Figure 5BE).To further
266 investigate such intra-tumoral heterogeneity, we assessed the Shannon Entropy between the models
267 in each core to measure the unanimity of single-cell predictions. A low entropy, close to zero, suggests
268 homogenous model predictions among all cells, which could either indicate systemic sensitivity or
269 systemic resistance. In contrast, higher values suggest a more heterogeneous, or random,
270 configuration of cell states, indicating a high diversity in distinct cells populations (Figure 7A). Overall,
271 we did not find a significant difference in model predictions with the majority of cores having high
272 entropy (> 0.5) for both models (Figure 7A). However, the cell composition of different cores may bias
273 the calculation if not stratified for cell types. While the difference was small, cancer cells and immune
274 cells had significantly lower entropy compared to stroma cells for DR_MOMP (Figure 7B). We found
275 something similar for the predictions of the APOPTO-CELL model, however, the difference between
276 cancer and immune cells was much more distinct (Figure 7C). Studying the entropy of protein levels
277 using histograms (normalized bin size = 0.1 SD) in cancer cells (Figure 7D), suggested the highest
278 entropy in BCL2 and the lowest entropy in MCL1 if comparing protein relevant for DR_MOMP. Among
279 proteins relevant for APOPTO-CELL, we found the highest entropy in XIAP and the lowest PRO-
280 CASPASE 3. Overall, cancer epithelial cells showed higher entropy in levels of all proteins but BCL(X)L
281 and PRO-CASPASE 3 when compered between epithelial cancer, immune and stroma cells (ANOVA p
282 < 0.05, Tukey post-hoc $p < 0.05$; Suppl. Figure 5). Figure 6D depicts examples of low (left) and high
283 (right) entropy. On average, protein levels of most proteins were greater in cancer compared to
284 immune and stroma cells (Figure 2) which allows more states and leads naturally to high entropy in
285 cancer cells.

286 We also assessed the presence of systematic spatial variation of protein levels and model predictions
287 (spatial autocorrelation) by measuring Moran's I in each core (Figure 7F-J). A Moran's I of 1 indicates
288 a perfect spatial separation (e.g. left *versus* right separation), while a value of -1 indicates a perfect

289 dispersion (checkerboard pattern; Figure 7F). A Moran's I is close to zero for a random distribution.
290 Figure 6G depicts examples of low (left) and high (right) Moran's I.

291 Overall, we found little evidence of strong spatial autocorrelation or spatial separation in the majority
292 of cores suggesting that cells that were close to each other did not have similar protein levels or similar
293 apoptosis sensitivities. Overall, we did not find any statistically significant difference in Moran's I
294 between the different apoptosis models (Figure 7H). Similar to the Entropy, this value is biased if cells
295 of different types are spatial separated, and Moran's I needs to be studied individually. Although we
296 observe only minor difference for the DR_MOMP model (Figure 7I), cancer cells with different
297 predictions for APOPTO-CELL were significantly more randomly dispersed compared to stromal cells
298 (ANOVA $p = 0.004$ and Tukey post-hoc $p = 0.002$; Figure 7E).

299 Calculating Moran's I for cells' protein levels, we found that the majority of cancer cells have a score
300 less than 0.2 suggesting a tendency towards a low correlation between protein level and the distance
301 between cells (Figure 7K). However, individual cores showed high spatial clustering for individual
302 protein suggesting that neighboring cells are more likely to have similar protein levels than distant
303 cells in these cores. Among the proteins relevant for DR_MOMP, BAX and BCL2 showed the higher
304 Moran's I compared to BAX, BCL(X)L and MCL1 (Figure 7K). Among proteins used in the APOPTO-CELL
305 model, SMAC had the lowest Moran's I compared to PRO-CASPASE 3, 9 and XIAP (Figure 7K). Of note,
306 since immune cells are more mobile than epithelial or stroma cells, we would assume to find the
307 lowest Moran's I in these cells. However, this was only the case for BAK, BCL2, PRO-CASPASE 3 and
308 GLUT1 (Suppl. Figure 6). While numerically different, overall the Moran's I was similar for BAX,
309 BCL(X)L, MCL1, SMAC and CA9 if stratified for cell types. We observed the greatest difference between
310 cells of different types for BAK, BCL2, GLUT1, HLA-I and KI67 (Suppl. Figure 6).

311 Collectively, intra-tumoural heterogeneity in apoptosis signaling was surprisingly not increased in
312 cancer cells when compared to leukocytes and other stromal cells, suggesting that heterogeneity in
313 apoptosis signaling represents an intrinsic, non-genomic cell property that is not increased by the
314 process of malignant transformation.

315 Discussion

316 The present study constitutes the first report describing the quantitative and spatial distribution of
317 key mitochondrial apoptosis proteins at single cell resolution in intact cancer tissue. Using multiplexed
318 immunofluorescence imaging (MxIF) we provide information on 2.4 million apoptosis protein profiles
319 in six different cell types and deliver the first atlas of apoptosis signaling proteins in a large cohort of

320 patients (164 colorectal cancer patients). We furthermore conducted a systems-based analysis of each
321 individual cell's apoptosis sensitivity. Our dynamic systems modelling estimated that cancer cells were
322 generally more sensitive to apoptosis signaling than immune or stromal cells, however with significant
323 heterogeneity between patients. We also characterized the level of intra-tumoral heterogeneity in
324 apoptosis signaling in colorectal cancer, and demonstrate that intra-tumoral heterogeneity in
325 apoptosis signaling was not increased in cancer cells when compared to leukocytes and other stromal
326 cells.

327 Apoptosis protein mapping in colorectal cancer and its implication for future therapy

328 Our first analysis steps constituted the mapping of protein profiles to the different cell types present
329 in the tumor microenvironment. Multiplexed protein imaging has been increasingly used as a tool for
330 spatial analysis of tumor cell types and microenvironment over the last 10 years (Angelo et al., 2014;
331 Gerdes et al., 2013; Goltsev et al., 2018; Gut et al., 2018; Kalra and Baker, 2017; Rashid et al., 2019;
332 Saka et al., 2019; Tan et al., 2020) and there are increasing number of multiplexing methods for in situ
333 RNA and DNA detection (Decalf et al., 2019; Kishi et al., 2019; Moffitt and Zhuang, 2016), Cell DIVE has
334 been used to analyze tumor cell heterogeneity in CRC (Badve et al., 2021; Spagnolo et al., 2017), ductal
335 carcinoma *in situ* (DCIS) (Badve et al., 2021; Gerdes et al., 2018), breast cancer (Sood et al., 2016),
336 glioma and glioblastoma (Berens et al., 2019) and melanoma (Yan et al., 2019). Unlike standard
337 immunohistochemistry methods which are limited to 1-5 markers in a single section, multiplexed
338 immunofluorescence imaging methods can provide single cell data on up to 60 proteins in a single
339 sample, including cell spatial coordinates, thus allowing analysis of co-expressed biomarkers and
340 relationships between cells types and functional status, as described in this paper.

341 Overall, we found that the 'average protein level' in a core (of the proteins we investigated), as
342 evaluated in bulk assays, is predominantly due to by the signal from cancer cells compared to immune
343 or stroma cells (Figure 2BE). However, among the analyzed key proteins regulating mitochondrial
344 apoptosis, we found interesting differences between the cell types (Figure 2AD). One of the key
345 findings was an enrichment in BCL-2 protein levels in immune cells when compared to cancer and
346 other stromal cells. This finding may have important implications regarding the use of BCL2
347 antagonists such as Venetoclax for the treatment of solid tumors. Venetoclax is well tolerated in
348 patients with relatively few side effects and would represent an ideal adjuvant and sensitizer to
349 chemotherapy for the treatment of chemotherapy-resistant solid tumors.

350 Nevertheless, Rohner *et al. (Rohner et al., 2020)* have previously shown that inhibition of BCL2 by ABT-
351 199 caused cell death in all types of lymphocytes but specifically reduced the counts of B cells in

352 humans. In addition, the authors showed that while T cells showed equivalent high levels of BCL2,
353 latter were significantly less affected compared to B cells, emphasizing that triggering apoptosis is "the
354 sum of the interplay of a network of anti- and pro-apoptotic BCL-2 family members" (Rohner et al.,
355 2020) and highlighting the importance of a systematical assessment of apoptosis. Our data suggest
356 that in certain patients BCL2 is also highly expressed in epithelial cancer cells, which could suggest that
357 BCL2 antagonist therapy may effectively reduce the overall anti-apoptotic threshold of cancer cells.
358 Due to complexity in cell-type specific BCL2 expression, our study suggests that evaluation of BCL2
359 levels in bulk tissues samples may not be sufficient as a stratification tools for BCL2 antagonists.

360 We found that MCL1 levels were enriched in epithelial and immune cells, with significantly lower levels
361 in stroma tissue. As MCL1 antagonists are also being currently developed as apoptosis sensitizers for
362 MCL-1-dependent cells, effects of MCL1 antagonists on immune cells may also need to be considered.
363 Of note, quantitatively, MCL1 levels were lower in cancer cells when compared to the anti-apoptotic
364 proteins BCL2 and BCL(X)L. Another interesting aspect of our study was the strong enrichment of BAK
365 in cancer cells. Recently, agents have been developed that activate BAX and BAK directly (Walensky
366 and Gavathiotis, 2011), including molecules that do not interact with the BH3-binding pocket of anti-
367 apoptotic proteins or pro-apoptotic BAK and induces cell death in a BAX-dependent fashion
368 (Gavathiotis et al., 2012; Gavathiotis et al., 2008). Our results suggest that BAK in particular is a good
369 target in colorectal cancer. Cancer cells also had significant higher levels of SMAC, XIAP and PRO-
370 CASPASE 9 compared to immune or stroma cells. It is therefore possible that colorectal tumors
371 expressing high XIAP levels in cancer cells are effectively sensitized by SMAC mimetics (Fichtner et al.,
372 2020), however analysis of both XIAP and SMAC levels may be required for future patient
373 stratification.

374 Priming of cancer cells and the degree of inter-individual heterogeneity

375 We also utilized the protein profiles for calculations of apoptosis sensitivity at the systems level.
376 Because of the complexity of apoptosis signaling with multiple signaling redundancies and feed-back
377 signaling, several groups have developed functional or computational models that describe apoptosis
378 sensitivity on a systems level. One such as approach, termed '*BH3-profiling*', interrogates the response
379 of the mitochondrial apoptosis pathway to pro-apoptotic BH3-only protein peptide mimetics (Certo
380 et al., 2006; Del Gaizo Moore and Letai, 2013; Montero and Letai, 2018). However, this technique
381 requires fresh tissue and living cells. To enable analysis of fresh frozen or formalin-fixed paraffin-
382 embedded tissue, we developed DR_MOMP (Lindner et al., 2013) as an ODE-based model of MOMP
383 that, similarly to BH3 profiling, calculates the response of the BCL2 signaling network to BH3-only
384 proteins activated upon cellular stress (Flanagan et al., 2015; Lindner et al., 2013; Lindner et al., 2017).

385 It has been extensively validated experimentally in colon and other cancer cells (Lindner et al., 2013;
386 Lindner et al., 2017; Lucantoni et al., 2018). Furthermore, we developed APOPTO-CELL as an ODE
387 model that calculates the sensitivity of cells to activate caspase-3 downstream of MOMP (Huber et al.,
388 2007; Rehm et al., 2006), as this process represents an important second control step. APOPTO-CELL
389 has also been extensively validated in-house using single cell imaging and population-based
390 approaches in cervical, colorectal and glioblastoma cells (Murphy et al., 2013; Salvucci et al., 2019a;
391 Salvucci et al., 2017; Schmid et al., 2012). Both models have also been shown to predict responses to
392 apoptosis sensitizers in preclinical settings (Lucantoni et al., 2018; O'Farrell et al., 2020). Our study
393 supports the previously developed concept that tumor cells are indeed 'primed' to undergo
394 mitochondrial apoptosis (Llambi et al., 2011; Ni Chonghaile et al., 2011). Including additional markers
395 for BH3-only proteins and caspase-independent cell death pathways will allow us to gain a more
396 holistic picture of possible cell fates in the future.

397 However, a surprising observation was that (based on model prediction) this appeared to result
398 predominantly from an enhanced ability to overcome both apoptosis barriers, MOMP and activation
399 of caspase-3 activation downstream of MOMP, as immune cells lack sensitivity for MOMP and other
400 stromal cells showed less sensitivity to caspase-3 activation (Figure 6AC). When comparing the ability
401 to undergo MOMP, cancerous cells were equally sensitive to stromal cells to undergo MOMP. In
402 contrast, immune cells appeared to be highly resistant to MOMP due to their relatively high expression
403 of increase in BCL2. Interestingly, we found that cytotoxic (CD8+) T cells were overall significantly more
404 susceptible to apoptosis stimuli compared to other immune cells. This is clinical relevant since tumor
405 infiltration by cytotoxic T Cells has been found to be significantly positively correlated with better
406 survival in colorectal cancer(Naito et al., 1998). In patients with breast cancer, changes in the ratio
407 between FOXP3+ (Regulatory) and CD8+ (cytotoxic) T cells (before and) after neoadjuvant
408 chemotherapy was highly associated with clinical response (Ladoire et al., 2008). Similarly, a low
409 density of cytotoxic T Cells in tumor tissue after chemotherapy was associated with poor response in
410 patients with rectal cancer (Matsutani et al., 2018). Therefore, increased risk of apoptosis of cytotoxic
411 T cells (e.g. following chemotherapy) may abrogate these benefits.

412 Nevertheless, our study cannot address the questions whether cancer cells are capable of activating
413 more BH3-only proteins at a given genotoxic (or metabolic) stress dose. We also observed significant
414 patient-to-patient heterogeneity in apoptosis sensitivity at both levels, while core-to-core differences
415 within single patients were less pronounced. Moreover, our combined analysis of both apoptosis
416 signaling pathways in each individual cell also allowed us to investigate potential blocks in either of
417 these pathways. Our combined analysis showed that the majority of cancer cells showed a high

418 sensitivity for at least one of the two apoptosis pathways up- and downstream of MOMP, which was
419 not observed to a similar degree in immune or other stromal cells.

420 Intra-tumoral heterogeneity

421 One of the limitations of the current study was that tumor core regions were analyzed, while tumor
422 margins in the invasive zone were not investigated. However other studies have pointed to the
423 importance of core regions in tumor progression due to silencing/methylation as a consequence of
424 tissue hypoxia (Thienpont et al., 2016). Based on this and other previous studies pointing to an
425 importance of intra-tumor heterogeneity in tumor progression and resistance, we also investigated
426 intra-tumor heterogeneity in apoptosis signaling. Collectively, our entropy and spatial image analyses
427 of the mitochondrial apoptosis pathway did not suggest that cancer cells showed an increased cell-to-
428 cell or spatial heterogeneity when compared to immune or other stromal cells. However, as shown in
429 the examples for Moran's I (Figure 7G), there can be a significant different between the value of 0.0
430 and 0.2 and assessing autocorrelation with alternative methods, such as Variograms, may be of
431 benefit. Another limitation was that we resolved the cell's phenotype in only three classes. Observed
432 heterogeneity in predicted model response and measured protein levels could arise through a high
433 number of various differentiated cells, and cells of the same type might have significantly lower
434 heterogeneity if compared among each other. Notwithstanding these limitations, our studies indicate
435 that intra-tumoral heterogeneity in apoptosis signaling was not increased in cancer cells, suggesting
436 that this represents an intrinsic, non-genomic property not increased by the process of malignant
437 transformation. This observation is supported by earlier studies in cell lines which demonstrated the
438 importance of non-genomic heterogeneity in apoptosis signaling due to fluctuations in protein levels
439 over the lifetime of a cell. Rehm *et al. (Rehm et al., 2009)* reported that sibling cells underwent
440 apoptosis execution within a narrow time window and that random cell pairs were significantly less
441 synchronous in undergoing apoptosis, independent of activating the intrinsic or extrinsic pathway.
442 However, the authors also reported that neither cell-to-cell distance nor cell membrane contacts
443 influenced the synchrony in apoptosis execution of sibling cells (Rehm et al., 2009). Similarly, Spencer
444 *et al. (Spencer et al., 2009)* previously showed that differences in the protein levels regulating
445 apoptosis are the primary causes of cell-to-cell variability in probability of death, with the protein state
446 being transmitted from mother to daughter, and protein synthesis rapidly promoting divergence
447 between these cells.

448 While we here consider the levels of 9 apoptosis markers, we did not take into account proteins' state
449 such as BCL2's phosphorylation status (Ruvolo et al., 2001) nor subcellular localization of proteins
450 which is possible to account for with the Cell DIVE™ platform. For example, BAX's localization at the

451 mitochondria or in the cytosol was reported to be clinically relevant in acute myeloid leukemia
452 (Reichenbach et al., 2017) and hepatocellular carcinoma (Funk et al., 2020). BAX localization could be
453 considered by including a mitochondrial marker, or by analyzing the BAX signal within the cytosolic
454 cell mask, with an evenly distributed signal suggesting cytosolic localization, and uneven distribution
455 suggesting localization at mitochondria.

456 In conclusion, our study provides the first map of apoptosis sensitivity at individual protein and
457 systems level in intact colorectal cancer tissue. We holistically describe both patient-to-patient and
458 intra-tumor heterogeneity in apoptosis signaling in stroma, immune and cancer cells which has
459 important implications for the future use of apoptosis sensitizers in the treatment of colorectal cancer.

460 Acknowledgments

461 This work was funded by a US-Northern Ireland-Ireland Tripartite grant from Science Foundation
462 Ireland and the Health Research Board to JHMP (16/US/3301) and the National Cancer Institute
463 (Systems Modeling of Tumor Heterogeneity and Therapy Response in Colorectal Cancer; to FG). EPO'C
464 is support by an RCSI Bon Secours Hospital MD StAR fellowship and the Beaumont Hospital Cancer
465 Research and Development Trust. DBL, PD, ML, XS were supported by US-Ireland R01 award (NI
466 Partner supported by HSCNI, STL/5715/15).

467 Author Contributions

468 AUL, MS, EMcD, SaCh, StCa, DPO'C, ADC, ASP, PLP, ML, AS, AS and JFG were involved in methodology,
469 data validation and curation. EMcD, SaCh, ADC, ASP, AS, JFG and FG performed the Cell DIVE
470 processing as well as cell segmentation and single cell quantification. AUL and MS statistically analyzed
471 the data and study investigation. JPB, DAmcN, SVS, JHMP, PLP, PD and DBL were involved in clinical
472 sample acquisition and data collection. EMcD AC and ASP conducted the sample imaging and image
473 processing. ASP and AS led the single cell analysis workflows for epithelial and immune cell analysis.
474 StCa and MF grow and processed the control cell lines. AUL, MS, JFG, SaCh, DBL, XS, FG and JHMP
475 reviewed the data. AUL, MS, MR, DBL, FG and JHMP designed experiments .AUL and JHMP wrote the
476 manuscript. AUL created the manuscript figures. MR, DBL, FG and JHMP were involved in funding
477 acquisition. All Authors edited and revised the manuscript text.

Declaration of Interests

The Cell DIVE™ platform was developed by GE Research. Sanghee Cho, Elizabeth McDonough, Anup Sood, John Graf, Alberto Santamaria-Pang, Alex Corwin and Fiona Ginty are all current and former employees of GE Research. The other authors have no potential conflicts.

482 # Figure titles and legends

483 Figure 1 – (A) Simplified workflow of the Cell DIVE™ platform and data analysis. (B) In total over 2
484 million cells, stratified into cancer, immune and stroma classes were analyzed. (C) Random forest was
485 used to differentiate cells using DAPI, and epithelial and CD markers. (D) The majority of cores
486 consisted of epithelial like cancer and stroma cells, (E) with less than 20% of cells being immune cells
487 in the majority of cores (ANOVA, Tukey post-hoc).

488 Figure 2 – Protein analysis of apoptosis proteins relevant for (A-C) the DR_MOMP model upstream of
489 MOMP and (D-F) the APOPTO-CELL model downstream of MOMP. (AD) To determine the difference
490 between protein quantification based on cell masks and quantification using the whole image, we first
491 determined the median protein concentration of each core, stratified for cancer (red), immune (blue)
492 and stroma (gray) cells (ANOVA, Tukey post-hoc). *x* marks panels with cropped high value outliers.
493 (BE) Subsequently, we compared the median pixel intensity of the core images (x-axes) with the
494 stratified median pixel intensities determined using cell masks (y-axes) before batch correction. The
495 scatter size indicates the numbers of stratified cells of the respective core. The panels C and F show
496 examples of the pre-batch corrected protein staining, cell type classification and batch corrected mean
497 cell intensities using cell masks.

498 Figure 3 – Global immune cell protein analysis of apoptosis proteins relevant for (A-C) the DR_MOMP
499 model upstream of MOMP and (D) the APOPTO-CELL model downstream of MOMP (ANOVA, Tukey
500 post-hoc). (B) Virtual IHC staining with BCL2 (red), CD3 (green) and CD45 (blue) shows that BCL2 level
501 vary largly between immune cells.

502 Figure 4 – (A) Protein analysis of KI67, CA9, GLUT1 and HLA_I proteins using core median protein levels
503 and stratified for cancer (red), immune (blue) and stroma (gray) cells (ANOVA, Tukey post-hoc). (B)
504 We compared the median pixel intensity of the core images (x-axes) with the stratified median pixel
505 intensities determined using cell masks (y-axes) before batch correction. The scatter size indicates the
506 numbers of stratified cells of the respective core. We calculated the median spearman correlation
507 coefficient between proteins, stratified for (C) cancer, (D) immune and (E) stroma cells. A more
508 detailed correplation plot, including inter quantile ranges, is provided as supplementary figure 4.

509 Figure 5 – Results of the cell-by-cell analysis using the apoptosis models DR_MOMP (Lindner et al.,
510 2013) and APOPTO-CELL (Huber et al., 2007; Rehm et al., 2006). (A) Graphical illustration of the
511 modelled BCL2 pathway (DR_MOMP) upstream of MOMP and the modelled caspase pathway
512 (APOPTO-CELL) downstream of MOMP. We first analyzed (B-D) DR_MOMP and subsequently (D-G)

513 APOPTO-CELL. (BE) First we determined model predictions of required stress to induce MOMP
514 (DR_MOMP) and % substrate cleavage upon MOMP (APOPTO-ELL) based on aggregated mean protein
515 level for each patient, using the pool of all cells of multiple cores. Subsequently we calculated the
516 cores' cell fractions with (B) high/low sensitivity for MOMP (DR_MOMP) and (E) high/low substrate
517 cleavage (APOPTO-CELL) using individual cell protein levels. We compared cores' fractions with
518 high/low (C) sensitivity for MOMP and (F) caspase activity stratified for cancer (red), immune (blue)
519 and stroma (gray) cells (ANOVA, Tukey post-hoc).The panels D and G show examples of individual
520 cores with high/low (D) sensitivity for MOMP and (G) caspase activity. In B and E, cores were sorted
521 from high apoptosis sensitivity (left) to low apoptosis sensitivity (right), respectively.

522 Figure 6 –We determined cores' cells that (A) exclusively showed high sensitivity for MOMP (left), high
523 caspase activity, high responses in both apoptosis pathways and low responses in both apoptosis
524 pathways (right; ANOVA, Tukey post-hoc).(BC) Ternary plot of individual core's cell fraction for
525 exclusively pathway responses or sensitivity in both pathways. Overall, cancer cells show high
526 sensitivity for the DR_MOMP modelled BCL2 pathway upstream of MOMP with about half showing
527 also high caspase activity modelled by APOPTO-CELL. Stroma cells showed exclusively high sensitivity
528 for the apoptosis pathway upstream for MOMP while immune cells showed exclusively high sensitivity
529 for MOMP.

530 Figure 7 – Heterogeneity analysis calculating cells' (A-E) Entropy and (F-K) Moran's I for apoptosis
531 model predictions as well protein levels. (A-E) Entropy (information theory) is a measurement for the
532 bias to one state, (A) with low entropy marking captaincy for a one state and high entropy marking
533 uncertainty for one or multiple states. We first determined the binary Shannon entropy for (B)
534 low/high sensitivity for MOMP (DR_MOMP) and (C) low/high caspase activity (APOPTO-CELL; ANOVA,
535 Tukey post-hoc), finding surprisingly significant lower entropy in cancer cells (red) compared to
536 immune (blue) and stroma cells (gray). (D) Subsequently, we calculated the Shannon Entropy for the
537 proteins using bins for protein level with a bin width of z-score = 0.1 SD for each protein respectively.
538 The calculated Shannon Entropy for stroma and Immune cells can be found in supplementary figure 5.
539 (E) shows examples with low (left) and high (right) entropy for the DR_MOMP model. (F) Moran's I is
540 a measurement of spatial autocorrelation with a Moran's I approaching 0 and < 0 indicating spatial
541 dispersion and a Moran's I approaching 1 marking spatial clustering. Panel G shows examples of
542 protein levels with low (left) and high (right) Moran's Is. (G-K) We determined cores' Moran's I for
543 low/high (I) sensitivity for MOMP, (J) caspase activity and (K) respective protein levels (in cancer cells).
544 Calculated Moran's I for Stroma and Immune cells can be found in supplementary figure 6. (G) While

545 a Moran's I around 0 shows no spatial autocorrelation, values around 0.2 or greater indicate presence
546 of local spatial autocorrelation within the cores.

547 STAR★Methods

548 Key Resource Table

REAGENT or RESEOURCE	SOURCE	IDENTIFIER or CONTACT	
Antibodies			
APAF-1	Millipore	2E12	MAB3053
Bak	Cell Signaling	D4E4	12105
Bax	Abcam	E63	ab216985
BCL-2	Lifespan	124	LS-C389442
Bcl-xL	Thermo	7D9	MS-1334
CA9	Thermo	polyclonal	PA1-16592
Caspase-3	Cell Signaling	D3R6Y	14214
Caspase-9	Santa Cruz	96.1.23	sc-56076 A647
CD3	Dako	F7.2.38	M7254
CD4	Abcam	EPR6855	ab181724
CD8	Dako	C8/144B	M7103
CD45	Dako	2B11 + PD7/26	M0701
Cytokeratin AE1	eBioscience	AE1	14-9001
Cytokeratin PCK26	Sigma	PCK26	C1801
FOXP3	Biolegend	206D	320014
Glut-1	Abcam	EPR3915	ab196357
HLA I	Abcam	EMR8 5	ab70328
Ki67	Zeta	SP6	Z2031
MCL-1	Abcam	Y37	ab186822
NAKATPase	Abcam	EP1845Y	ab167390
S6	Santa Cruz	C-8	sc-74459 A647
Smac	Cell Signaling	79-1-83	2954
PD1	Abcam	EPR4877(2)	ab201825
XIAP (API3)	Thermo	polyclonal	APH937
Cell Lines			
HCT-116 SMAC KO	Dr. B Vogelstein (John Hopkins University, MD, USA)		
HCT-116 XIAP KO	Dr. B Vogelstein (John Hopkins University, MD, USA)		
HeLa	American Type Culture Collection (LGC Standards)		
JURKAT	Dr. PH Krammer and Dr. H Walczak (DKFZ, Germany)		
MCF7	Dr. RU Jänicke (University of Düsseldorf, Germany)		
SKMEL	DSMZ, Germany	ACC 151	

REAGENT or RESEOURCE	SOURCE	IDENTIFIER or CONTACT
Biological Samples		
Stage III primary CRC tumour tissue resect prior 5-FU based chemotherapy	Beaumont Hospital (RCSI, IE)	*NA*
	Queen's University Belfast (UK)	*NA*
	Paris Descartes University (FR)	*NA*
Cell DIVE Platform		
Cell DIVE™	Cytiva; GE Research	fiona.ginty@ge.com
Multi tumor tissue array	Pantomics	MTU 481
Software and algorithms		
R (3.6.3)	R Foundation	www.r-project.org
Fiji (ImageJ; 1.51k)	Schindelin *et al.*(Schindelin et al., 2012)	www.fiji.sc
GE SingleCellMetrics Plugin	GE Research	fiona.ginty@ge.com
Layers cell analysis software version 1	GE Research	fiona.ginty@ge.com
APOPTO-CELL	Rehm and Huber *et al.*(Huber et al., 2007; Rehm et al., 2006)	prehn@rcsi.ie
DR_MOMP	Lindner *et al.*(Lindner et al., 2013)	prehn@rcsi.ie
MATLAB with the Statistics and Parallel toolboxes (version 2014b)	The MathWorks	www.mathworks.com

Resource Availability

Lead Contact

Further information and request for code or resources should be directed to and will be fulfilled by the lead contact, Prof. Jochen Prehn (prehn@rcsi.ie).

Materials Availability

- This study did not generate new unique reagents.

Data and Code Availability

- Imaging data, cell masks and generated single cell measurements of 20 markers is available from the lead contact.
- The full pipeline for data analysis is available from the lead contact.
- Any additional information required to reproduce this work is available from the Lead Contact.

Experimental Model and Subject Details

This section does not apply to our computational study.

Method Details

Colorectal cancer cohort

Formalin-fixed, paraffin-embedded (FFPE) primary tumor tissue sections were obtained from 170 chemotherapy-naïve, resected stage III CRC patients. Tumor samples were collected from three centers: Beaumont Hospital (RCSI, Ireland), Queen's University Belfast (UK) and Paris Descartes University (France). All centers provided ethical approval for this study and informed consent was obtained from all participants. A summary of the clinical characteristics of the cohort is provided in Suppl. Table 1. Data of 46 cores of 36 patients were dropped after quality assessment of the stained tissue (see below). All cores of two patients were removed in this process.

Cell lines

Three technical replicates (cores) of pellets of formalin-fixed HeLa, Jurkat, MCF7, SKMEL, HCT-116 $SMAC^{KO}$ and HCT-116 $XIAP^{KO}$ cells in which quantities of mitochondrial apoptosis proteins were previously determined (Lindner et al., 2013; Passante et al., 2013; Rehm et al., 2006) were included in the construction of the tissue microarray (TMA) in parallel to the patients' cores, and served as quality control and internal standards for protein quantification. 3 of 18 cores of two cell lines were removed after quality control. Cells were grown to 80% confluence. Media was replaced 12-24 hours before fixation. To fix cells, cells were gently washed in sterile 1XPBS solution. Cell monolayers were covered with 5 mL 10% neutral-buffered formalin (NBF) for 2-5 min. Cells were scraped into NBF, and collected into labelled 50 mL tubes, and stored at 4 C for at least 3-4 hours. For further processing, cells were centrifuged at 1,200 rpm for 5 min and washed in 1% low melt agarose solution XBPS before re-suspension in 0.5 ml 80% ethanol and centrifugation at 12,000 rpm twice for 5 min. Subsequently 80% of ethanol was aspirated and cell pellets were molded into caps and frozen, prior to TMA construction.

Antibody validation and conjugation

Commercially acquired antibodies underwent multi-step process of validation and conjugation (as previously described by Gerdes *et al.* (Gerdes et al., 2013). Briefly, at least 2-3 clones for each target were stained in parallel using a multi-tissue array (MTU 481, Pantomics, CA) and staining performance visually compared. At least one antibody clone was down-selected for conjugation with either Cy3 or Cy5 bis-NHS-ester dyes. Epitopes were also tested for sensitivity to the dye inactivation solution (basic

590 hydrogen peroxide) by exposing multi-tissue arrays to 0, 1 and 10 rounds the solution and stained with
591 the antibody of interest and compared. Approx. 10% of epitopes have been shown to have decreased
592 signal following exposure to the inactivation solution and those antibodies are placed early in the
593 multiplexing sequence (Gerdes et al., 2013). The key resource table shows the antibodies, clones and
594 conjugates used in this study. Briefly the markers and staining rounds were as follows: Round 1: BCL2,
595 APAF1; Round 2: MCL1, PRO-CASPASE-9; Round 3: S6, PRO-CASPASE-3; Round 4: BAX, SMAC; Round
596 5: BAK, XIAP; Round 6: NaKATPase, BCL(X)L; Round 7: Cytokeratin PCK26, CD8; Round 8: Cytokeratin
597 AE1, FOXP3; Round 9: CD4, Ki67; Round 10: HLA1, CD45; Round 11: Glut1, CA9; Round 12: CD3, PD1;
598 Round 13: S6 (repeated). Note that in total, 9 background imaging rounds were also included.

599 Immunofluorescence Imaging of Patient TMAs

600 Multiplexed immunofluorescence iterative staining of the CRC TMAs was performed as previously
601 described (Gerdes et al., 2013) using the Cell DIVE™ technology (Cytiva, Issaquah, WA; formerly GE
602 Healthcare). This involves iterative staining and imaging of the same tissue section with 60+ antibodies
603 and is achieved by mild dye oxidation between successive staining and imaging rounds. In total, there
604 were 13 staining rounds using the antibodies described above and DAPI was imaged in each round.
605 The Leica Bond (Leica Biosystems) was used for antibody staining and the IN Cell 2200 was used for
606 imaging. Staining and image recording was repeated twice for S6 due to staining failure. Exposure
607 times were set to fixed values for all images of a given marker.

608 Image pre-processing

609 Immunofluorescent images were processed and cells were segmented and quantified as described
610 previously (Gerdes et al., 2013). To summarize, cells in the epithelial and stromal compartments were
611 segmented using DAPI, pan-cytokeratin, S6, and NaKATPase stains (Gerdes et al., 2013). Images and
612 segmented cell data then underwent a multistep review process (described by Berens et al.(Berens et
613 al., 2019): 1) images were visually reviewed and manual scoring of tissue quality and segmentation
614 was determined by at least one researcher. Images with poor quality staining or too few cells were
615 excluded from data analysis; 2) cell filtering based on minimum and maximum number of pixels in
616 each sub-cellular compartment (> 10 pixels and < 1500 pixels per compartment) and 1-2 nuclei per
617 cell; cells with values outside these limits were removed 3) confirmation of excellent alignment of all
618 cells in all staining rounds compared to the first round of staining. For this, an automated QC score
619 was generated for every cell in each imaging round by correlating baseline DAPI images with all
620 corresponding DAPI images from other multiplexing rounds. A perfect score of 1 indicated perfect
621 registration, no cell loss and no cell movement. A score of 0 indicated complete loss of that cell after

622 baseline imaging. After quality control, cells included in the analysis had a median QC score of 0.95,
623 with 53% having a QC score greater than 0.8. The average QC score was 0.57. In comparison, 83% of
624 cells removed during quality control had a QC score less than 0.1 with an average QC score of 0.15.
625 From the single-cell segmentation masks, the mean intensity, standard deviation, and coherent
626 statistics were quantified for each protein with respect to the whole cell as well as xy-location. From
627 the single-cell segmentation masks, the mean, standard deviation, median, and maximum staining
628 intensity for each protein were quantified with respect to the whole cell, cell membrane, cytoplasm,
629 and nucleus as well as cell location, area, and shape. Following quantification, slides were normalized
630 for batch effects and exposure time for each channel/marker analyzed.

631 48 positions showing major cell loss during staining rounds were excluded from all analysis, as well as
632 cells within the images' margins of 15 pixel on the x-axis and 10 pixel on the y-axes were dropped from
633 all data analysis. 74 positions showing major or minor cell loss during staining rounds were excluded
634 from training datasets for post-processing such as batch correction or cell classification.

635 Post pre-processing and batch correction

636 To correct for a possible batch effects between slides, cells' mean intensity were first normalized using
637 upper-quantile normalization, grouped by protein marker and slide. Secondly, quantiles of the
638 normalized intensities were plotted against their rankits, and an affine transformation matrices to
639 rotate the function to the main diagonal were calculated. Obtained transformation matrices were
640 applied on the intensities, and pixel intensity values were restored using linear regression and upper-
641 quantile normalized values. Solely for the batch correction, cells within 5% of the images' margins
642 were excluded for the calculation of the reference values. The batch correction was quality controlled
643 with cell lines spotted in parallel to tissue samples on 3 of 5 slides.

644 Immune Cell classification

645 To differentiate cell types, we used CD3, CD4, CD8, CD45, FOXP3, PCK26 and Cytokeratin AE1 markers.
646 We manually annotated 4,839 AE1- or PCK27-positive cells as (epithelial) cancer cells. Of 3,121 CD3-
647 positive cells (Beare et al., 2008), 788 CD4-positive cells were annotated as Helper T cells (Beare et al.,
648 2008), 991 CD8-positive cells were annotated as Cytotoxic T cells (Beare et al., 2008), and
649 1,360 FOXP3-positive cells were annotated as Regulatory T cells (Hori et al., 2003). 3,369 CD3-negative
650 cells that were either CD4-, CD45- or CD8-positive were annotated as other leukocytes. 3,837 cells
651 that lacked any marker but were DAPI positive were annotated as stroma-rich cells (other stromal
652 cells). Using the manual annotations, we constructed a random forest of 2,000 trees (R package
653 *randomForest*, version 4.6-14) and employed it to classify all cells.

654 # Protein profiling and apoptosis sensitivity modelling

655 Protein levels of BAK, BAX, BCL2, BCL(X)L and MCL1 were normalized to the mean protein levels in
656 HeLa cells spotted in parallel to patients' core on 3 of 5 slides. Protein's molar concentrations were
657 calculated using previously established HeLa concentrations (Lindner et al., 2013).The five proteins
658 were used as input for the DR_MOMP mathematical model(Lindner et al., 2013) that models the BCL2
659 signaling pathway before MOMP and is able to calculate the stress dose required for MOMP or if a cell
660 undergoes MOMP due to a specified stress. DR_MOMP (Lindner et al., 2013) was translated from its
661 MATLAB implementation to C++ and R using deSolve (1.28), doParallel (1.0.15) and Rcpp (1.0.5).

662 APOPTO-CELL (Rehm et al., 2006) was executed in MATLAB with the *Statistics and Parallel toolboxes*
663 (version 2014b, The MathWorks, Inc., Natick, MA, USA). The model requires molar concentrations
664 [μM] of APAF1, PRO-CASPASE 3, PRO-CASPASE 9, SMAC and XIAP as input to predict amount of
665 cleaved substrate, as a readout for apoptosis susceptibility [%]. Previous research(Hector et al., 2012;
666 Salvucci et al., 2019a) has shown that APAF1 is not the limiting factor in apoptosome formation in the
667 CRC settings(Hector et al., 2012; Salvucci et al., 2019a) and was set to 0.123 μM. Molar protein
668 concentrations for PRO-CASPASE 3, PRO-CASPASE 9, SMAC and XIAP were estimated by aligning signal
669 intensities [a.U.] to profiles [μM] determined in a reference clinically-relevant CRC cohort(Hector et
670 al., 2012) with an established pipeline(Salvucci et al., 2019a; Salvucci et al., 2017). The pipeline was
671 built upon the assumptions that 1) measurement ranking is preserved (monotonic relationship
672 between batch-corrected signaling intensities and molar concentrations); and 2) absolute
673 concentration profiles in clinically-matched cohorts are comparable. The pipeline implementation
674 follows directly from the above assumptions. Briefly, for each protein smoothed kernel probability
675 distribution objects were fitted to 1) the known protein molar concentrations of the reference CRC
676 cohort (Hector et al., 2012) and 2) batch-corrected multiplexed signal intensities (restricted to high
677 quality data points where no signal loss across staining rounds had been observed), with the MATLAB
678 function *fitdist (*as detailed in Salvucci M *et al. (Salvucci et al., 2017)*). The inverse cumulative
679 distribution transformation of the reference distribution kernel was applied on the batch-corrected
680 signal intensities to determine the corresponding absolute concentrations (MATLAB function *icdf*).

681 For both models, we performed two sets of simulations: 1) per-core and 2) per-cell. For the per-core
682 simulations, we aggregated (by median) the batch-corrected protein intensities across all cells for each
683 core per patient prior to conversion to molar concentrations, resulting in one simulations per-core
684 and thus 2-3 simulations per patient. For the per-cell simulations, we performed a simulation for each
685 cell, totaling ~3.5 million simulations for 164 patients included in the study.

686 ## Statistical Analysis

687 All statistical tests were performed in R (3.6.3) and p values of < 0.05 were considered statistically
688 significant. All data are presented as mean ± SEM. All statistical tests were performed in R. If not
689 otherwise mentioned, two-tailed t tests were performed for pairwise comparison, while analysis of
690 variance (ANOVA) with Tukey honest significance post-hoc tests were performed in cases of the
691 comparison of three or more populations. The quartile coefficients of dispersion (COF) were calculated
692 using $(Q_3 - Q_1) / (Q_3 + Q_1)$ with Q_n be the respective quartiles. Shannon Entropy was calculated either
693 using $\log_2$ for binary populations or the natural logarithm, with 10^{-10} added to all values. Moran's I was
694 calculated using the R package *ape* (5.4-1) without outliers and only on populations > 100 cells.
695 Distances > 2,000 px were set to 2,000 px. Consensus Clustering was performed using
696 *ConsensusClusterPlus* (1.48.0) with a seed of 42, 100,000 repetitions, Spearman and Ward's method
697 as parameters. For the bootstrap analysis, slides were randomly 100,000 times randomly paired using
698 a seed of 42.

699 Supplemental Information titles and legends

700 Supplementary Table 1 – Patient information with mean cell fractions and DR_MOMP and APOPTO-
701 CELL results for aggregated protein levels for patient-matched cores.

702 Supplementary Table 2 - of transcriptional data derived from flow-sorted immune, epithelial and
703 fibroblast populations isolated from CRC primary tumor tissue (GSE39396).

704 Supplementary Figure 1 - Plot of patients' consensus cluster score of patient-matched cores after
705 hierarchical consensus clustering using cancer, immune and stroma cell fractions of each core.
706 Patients with a low consensus score (0) show high difference in cell fractions between matched cores
707 while patients with a high consensus score (1) show high similarity in cell fractions between matched
708 cores.

709 Supplementary Figure 2 – Box plot of transcriptional data derived from flow-sorted immune (n = 6),
710 epithelial (n = 6) and fibroblast (n = 6) populations isolated from CRC primary tumor tissue (GSE39396
711 (Calon et al., 2012); Suppl. Table 2; ANOVA and Tukey post-hoc).

712 Supplementary Figure 3 - Box plot of quartile coefficients of dispersion of protein levels of each core
713 and stratified for cancer (red), immune (blue) and stroma cells (grey).

714 Supplementary Figure 4 - In analog to the correlation plot in Figure 4C-E showing the median
715 correlation coefficient in all (black), cancer (red), immune (blue) and stroma (gray) cells, but including
716 the interquartile range.

717 Supplementary Figure 5 - Calculated the Shannon Entropy for the proteins using bins for protein level
718 with a bin width of z-score = 0.1 SD for each protein respectively and stratified for cancer (red),
719 immune (blue) and stroma (gray) cells. Proteins were sorted base for (A) DR_MOMP, (B) APOPTO-CELL
720 and (C) others.

721 Supplementary Figure 6 - Calculated cores' Moran's I for low/high (I) sensitivity for MOMP for protein
722 levels stratified for cancer (red), immune (blue) and stroma (gray) cells. Proteins were sorted base for
723 (A) DR_MOMP, (B) APOPTO-CELL and (C) others.

References

Angelo, M., Bendall, S.C., Finck, R., Hale, M.B., Hitzman, C., Borowsky, A.D., Levenson, R.M., Lowe, J.B., Liu, S.D., Zhao, S.*, et al.* (2014). Multiplexed ion beam imaging of human breast tumors. Nat Med *20*, 436-442.

Badve, S.S., Cho, S., Gökmen-Polar, Y., Sui, Y., Chadwick, C., McDonough, E., Sood, A., Taylor, M., Zavodszky, M., Tan, P.H.*, et al.* (2021). Multi-protein spatial signatures in ductal carcinoma in situ (DCIS) of breast. Br J Cancer.

Beare, A., Stockinger, H., Zola, H., and Nicholson, I. (2008). Monoclonal antibodies to human cell surface antigens. Curr Protoc Immunol *Appendix 4*, 4A.

Berdasco, M., and Esteller, M. (2010). Aberrant epigenetic landscape in cancer: how cellular identity goes awry. Dev Cell *19*, 698-711.

Berens, M.E., Sood, A., Barnholtz-Sloan, J.S., Graf, J.F., Cho, S., Kim, S., Kiefer, J., Byron, S.A., Halperin, R.F., Nasser, S.*, et al.* (2019). Multiscale, multimodal analysis of tumor heterogeneity in IDH1 mutant vs wild-type diffuse gliomas. PLoS One *14*, e0219724.

Calon, A., Espinet, E., Palomo-Ponce, S., Tauriello, D.V., Iglesias, M., Céspedes, M.V., Sevillano, M., Nadal, C., Jung, P., Zhang, X.H.*, et al.* (2012). Dependency of colorectal cancer on a TGF-β-driven program in stromal cells for metastasis initiation. Cancer Cell *22*, 571-584.

Certo, M., Del Gaizo Moore, V., Nishino, M., Wei, G., Korsmeyer, S., Armstrong, S.A., and Letai, A. (2006). Mitochondria primed by death signals determine cellular addiction to antiapoptotic BCL-2 family members. Cancer Cell *9*, 351-365.

Decalf, J., Albert, M.L., and Ziai, J. (2019). New tools for pathology: a user's review of a highly multiplexed method for in situ analysis of protein and RNA expression in tissue. J Pathol *247*, 650-661.

Del Gaizo Moore, V., and Letai, A. (2013). BH3 profiling--measuring integrated function of the mitochondrial apoptotic pathway to predict cell fate decisions. Cancer Lett *332*, 202-205.

Fichtner, M., Bozkurt, E., Salvucci, M., McCann, C., McAllister, K.A., Halang, L., Düssmann, H., Kinsella, S., Crawford, N., Sessler, T.*, et al.* (2020). Molecular subtype-specific responses of colon cancer cells to the SMAC mimetic Birinapant. Cell Death Dis *11*, 1020.

Fisher, R., Pusztai, L., and Swanton, C. (2013). Cancer heterogeneity: implications for targeted therapeutics. Br J Cancer *108*, 479-485.

Flanagan, L., Lindner, A.U., de Chaumont, C., Kehoe, J., Fay, J., Bacon, O., Toomey, S., Huber, H.J., Hennessy, B.T., Kay, E.W.*, et al.* (2015). BCL2 protein signalling determines acute responses to neoadjuvant chemoradiotherapy in rectal cancer. J Mol Med (Berl) *93*, 315-326.

Funk, K., Czauderna, C., Klesse, R., Becker, D., Hajduk, J., Oelgeklaus, A., Reichenbach, F., Fimm-Todt, F., Lauterwasser, J., Galle, P.R.*, et al.* (2020). BAX Redistribution Induces Apoptosis Resistance and Selective Stress Sensitivity in Human HCC. Cancers (Basel) *12*.

Gavathiotis, E., Reyna, D.E., Bellairs, J.A., Leshchiner, E.S., and Walensky, L.D. (2012). Direct and selective small-molecule activation of proapoptotic BAX. Nat Chem Biol *8*, 639-645.

761 Gavathiotis, E., Suzuki, M., Davis, M.L., Pitter, K., Bird, G.H., Katz, S.G., Tu, H.C., Kim, H., Cheng, E.H.,
762 Tjandra, N.*, et al.* (2008). BAX activation is initiated at a novel interaction site. Nature *455*, 1076-1081.

763 Gerdes, M.J., Gökmen-Polar, Y., Sui, Y., Pang, A.S., LaPlante, N., Harris, A.L., Tan, P.H., Ginty, F., and
764 Badve, S.S. (2018). Single-cell heterogeneity in ductal carcinoma in situ of breast. Mod Pathol *31*, 406-
765 417.

766 Gerdes, M.J., Sevinsky, C.J., Sood, A., Adak, S., Bello, M.O., Bordwell, A., Can, A., Corwin, A., Dinn, S.,
767 Filkins, R.J.*, et al.* (2013). Highly multiplexed single-cell analysis of formalin-fixed, paraffin-embedded
768 cancer tissue. Proc Natl Acad Sci U S A *110*, 11982-11987.

769 Goltsev, Y., Samusik, N., Kennedy-Darling, J., Bhate, S., Hale, M., Vazquez, G., Black, S., and Nolan, G.P.
770 (2018). Deep Profiling of Mouse Splenic Architecture with CODEX Multiplexed Imaging. Cell *174*, 968-
771 981.e915.

772 Gut, G., Herrmann, M.D., and Pelkmans, L. (2018). Multiplexed protein maps link subcellular
773 organization to cellular states. Science *361*.

774 Hanahan, D., and Weinberg, R.A. (2011). Hallmarks of cancer: the next generation. Cell *144*, 646-674.

775 Hector, S., Rehm, M., Schmid, J., Kehoe, J., McCawley, N., Dicker, P., Murray, F., McNamara, D., Kay,
776 E.W., Concannon, C.G.*, et al.* (2012). Clinical application of a systems model of apoptosis execution for
777 the prediction of colorectal cancer therapy responses and personalisation of therapy. Gut *61*, 725-
778 733.

779 Hori, S., Nomura, T., and Sakaguchi, S. (2003). Control of regulatory T cell development by the
780 transcription factor Foxp3. Science *299*, 1057-1061.

781 Huber, H.J., Rehm, M., Plchut, M., Dussmann, H., and Prehn, J.H. (2007). APOPTO-CELL--a simulation
782 tool and interactive database for analyzing cellular susceptibility to apoptosis. Bioinformatics *23*, 648-
783 650.

784 Ichim, G., and Tait, S.W. (2016). A fate worse than death: apoptosis as an oncogenic process. Nat Rev
785 Cancer *16*, 539-548.

786 Kalkavan, H., and Green, D.R. (2018). MOMP, cell suicide as a BCL-2 family business. Cell Death Differ
787 *25*, 46-55.

788 Kalra, J., and Baker, J. (2017). Multiplex Immunohistochemistry for Mapping the Tumor
789 Microenvironment. Methods Mol Biol *1554*, 237-251.

790 Kishi, J.Y., Lapan, S.W., Beliveau, B.J., West, E.R., Zhu, A., Sasaki, H.M., Saka, S.K., Wang, Y., Cepko, C.L.,
791 and Yin, P. (2019). SABER amplifies FISH: enhanced multiplexed imaging of RNA and DNA in cells and
792 tissues. Nat Methods *16*, 533-544.

793 Ladoire, S., Arnould, L., Apetoh, L., Coudert, B., Martin, F., Chauffert, B., Fumoleau, P., and Ghiringhelli,
794 F. (2008). Pathologic complete response to neoadjuvant chemotherapy of breast carcinoma is
795 associated with the disappearance of tumor-infiltrating foxp3+ regulatory T cells. Clin Cancer Res *14*,
796 2413-2420.

797 Leber, B., Lin, J., and Andrews, D.W. (2007). Embedded together: the life and death consequences of
798 interaction of the Bcl-2 family with membranes. Apoptosis *12*, 897-911.

799 Lindner, A.U., Concannon, C.G., Boukes, G.J., Cannon, M.D., Llambi, F., Ryan, D., Boland, K., Kehoe, J.,
800 McNamara, D.A., Murray, F.*, et al.* (2013). Systems analysis of BCL2 protein family interactions
801 establishes a model to predict responses to chemotherapy. Cancer Res *73*, 519-528.

802 Lindner, A.U., Salvucci, M., Morgan, C., Monsefi, N., Resler, A.J., Cremona, M., Curry, S., Toomey, S.,
803 O'Byrne, R., Bacon, O.*, et al.* (2017). BCL-2 system analysis identifies high-risk colorectal cancer
804 patients. Gut *66*, 2141-2148.

805 Llambi, F., Moldoveanu, T., Tait, S.W., Bouchier-Hayes, L., Temirov, J., McCormick, L.L., Dillon, C.P.,
806 and Green, D.R. (2011). A unified model of mammalian BCL-2 protein family interactions at the
807 mitochondria. Mol Cell *44*, 517-531.

808 Lucantoni, F., Lindner, A.U., O'Donovan, N., Düssmann, H., and Prehn, J.H.M. (2018). Systems modeling
809 accurately predicts responses to genotoxic agents and their synergism with BCL-2 inhibitors in triple
810 negative breast cancer cells. Cell Death Dis *9*, 42.

811 Marusyk, A., Almendro, V., and Polyak, K. (2012). Intra-tumour heterogeneity: a looking glass for
812 cancer? Nat Rev Cancer *12*, 323-334.

813 Matsutani, S., Shibutani, M., Maeda, K., Nagahara, H., Fukuoka, T., Nakao, S., Hirakawa, K., and Ohira,
814 M. (2018). Significance of tumor-infiltrating lymphocytes before and after neoadjuvant therapy for
815 rectal cancer. Cancer Sci *109*, 966-979.

816 Mauro, J.A., Butler, S.N., Ramsamooj, M., and Blanck, G. (2015). Copy number loss or silencing of
817 apoptosis-effector genes in cancer. Gene *554*, 50-57.

818 Moffitt, J.R., and Zhuang, X. (2016). RNA Imaging with Multiplexed Error-Robust Fluorescence In Situ
819 Hybridization (MERFISH). Methods Enzymol *572*, 1-49.

820 Montero, J., and Letai, A. (2018). Why do BCL-2 inhibitors work and where should we use them in the
821 clinic? Cell Death Differ *25*, 56-64.

822 Murphy, Á., Weyhenmeyer, B., Schmid, J., Kilbride, S.M., Rehm, M., Huber, H.J., Senft, C.,
823 Weissenberger, J., Seifert, V., Dunst, M.*, et al.* (2013). Activation of executioner caspases is a predictor
824 of progression-free survival in glioblastoma patients: a systems medicine approach. Cell Death Dis *4*,
825 e629.

826 Naito, Y., Saito, K., Shiiba, K., Ohuchi, A., Saigenji, K., Nagura, H., and Ohtani, H. (1998). CD8+ T cells
827 infiltrated within cancer cell nests as a prognostic factor in human colorectal cancer. Cancer Res *58*,
828 3491-3494.

829 Ni Chonghaile, T., Sarosiek, K.A., Vo, T.T., Ryan, J.A., Tammareddi, A., Moore, V.e.G., Deng, J.,
830 Anderson, K.C., Richardson, P., Tai, Y.T.*, et al.* (2011). Pretreatment mitochondrial priming correlates
831 with clinical response to cytotoxic chemotherapy. Science *334*, 1129-1133.

832 O'Farrell, A.C., Jarzabek, M.A., Lindner, A.U., Carberry, S., Conroy, E., Miller, I.S., Connor, K., Shiels, L.,
833 Zanella, E.R., Lucantoni, F.*, et al.* (2020). Implementing Systems Modelling and Molecular Imaging to
834 Predict the Efficacy of BCL-2 Inhibition in Colorectal Cancer Patient-Derived Xenograft Models. Cancers
835 (Basel) *12*.

836 Passante, E., Würstle, M.L., Hellwig, C.T., Leverkus, M., and Rehm, M. (2013). Systems analysis of
837 apoptosis protein expression allows the case-specific prediction of cell death responsiveness of
838 melanoma cells. Cell Death Differ *20*, 1521-1531.

839 Rashid, R., Gaglia, G., Chen, Y.A., Lin, J.R., Du, Z., Maliga, Z., Schapiro, D., Yapp, C., Muhlich, J., Sokolov,
840 A.*, et al.* (2019). Highly multiplexed immunofluorescence images and single-cell data of immune
841 markers in tonsil and lung cancer. Sci Data *6*, 323.

842 Rehm, M., Huber, H.J., Dussmann, H., and Prehn, J.H. (2006). Systems analysis of effector caspase
843 activation and its control by X-linked inhibitor of apoptosis protein. EMBO J *25*, 4338-4349.

844 Rehm, M., Huber, H.J., Hellwig, C.T., Anguissola, S., Dussmann, H., and Prehn, J.H. (2009). Dynamics of
845 outer mitochondrial membrane permeabilization during apoptosis. Cell Death Differ *16*, 613-623.

846 Reichenbach, F., Wiedenmann, C., Schalk, E., Becker, D., Funk, K., Scholz-Kreisel, P., Todt, F.,
847 Wolleschak, D., Döhner, K., Marquardt, J.U.*, et al.* (2017). Mitochondrial BAX Determines the
848 Predisposition to Apoptosis in Human AML. Clin Cancer Res *23*, 4805-4816.

849 Roberts, A.W., Davids, M.S., Pagel, J.M., Kahl, B.S., Puvvada, S.D., Gerecitano, J.F., Kipps, T.J.,
850 Anderson, M.A., Brown, J.R., Gressick, L.*, et al.* (2016). Targeting BCL2 with Venetoclax in Relapsed
851 Chronic Lymphocytic Leukemia. N Engl J Med *374*, 311-322.

852 Rohner, L., Reinhart, R., Iype, J., Bachmann, S., Kaufmann, T., and Fux, M. (2020). Impact of BH3-
853 mimetics on Human and Mouse Blood Leukocytes: A Comparative Study. Sci Rep *10*, 222.

854 Ruvolo, P.P., Deng, X., and May, W.S. (2001). Phosphorylation of Bcl2 and regulation of apoptosis.
855 Leukemia *15*, 515-522.

856 Saka, S.K., Wang, Y., Kishi, J.Y., Zhu, A., Zeng, Y., Xie, W., Kirli, K., Yapp, C., Cicconet, M., Beliveau, B.J.*,*
857 *et al.* (2019). Immuno-SABER enables highly multiplexed and amplified protein imaging in tissues. Nat
858 Biotechnol *37*, 1080-1090.

859 Salvucci, M., Rahman, A., Resler, A.J., Udupi, G.M., McNamara, D.A., Kay, E.W., Laurent-Puig, P.,
860 Longley, D.B., Johnston, P.G., Lawler, M.*, et al.* (2019a). A Machine Learning Platform to Optimize the
861 Translation of Personalized Network Models to the Clinic. JCO Clin Cancer Inform *3*, 1-17.

862 Salvucci, M., Wurstle, M.L., Morgan, C., Curry, S., Cremona, M., Lindner, A.U., Bacon, O., Resler, A.J.,
863 Murphy, A.C., O'Byrne, R.*, et al.* (2017). A Stepwise Integrated Approach to Personalized Risk
864 Predictions in Stage III Colorectal Cancer. Clin Cancer Res *23*, 1200-1212.

865 Salvucci, M., Zakaria, Z., Carberry, S., Tivnan, A., Seifert, V., Kögel, D., Murphy, B.M., and Prehn, J.H.M.
866 (2019b). System-based approaches as prognostic tools for glioblastoma. BMC Cancer *19*, 1092.

867 Schindelin, J., Arganda-Carreras, I., Frise, E., Kaynig, V., Longair, M., Pietzsch, T., Preibisch, S., Rueden,
868 C., Saalfeld, S., Schmid, B.*, et al.* (2012). Fiji: an open-source platform for biological-image analysis. Nat
869 Methods *9*, 676-682.

870 Schmid, J., Dussmann, H., Boukes, G.J., Flanagan, L., Lindner, A.U., O'Connor, C.L., Rehm, M., Prehn,
871 J.H., and Huber, H.J. (2012). Systems analysis of cancer cell heterogeneity in caspase-dependent
872 apoptosis subsequent to mitochondrial outer membrane permeabilization. J Biol Chem *287*, 41546-
873 41559.

874 Sood, A., Miller, A.M., Brogi, E., Sui, Y., Armenia, J., McDonough, E., Santamaria-Pang, A., Carlin, S.,
875 Stamper, A., Campos, C.*, et al.* (2016). Multiplexed immunofluorescence delineates proteomic cancer
876 cell states associated with metabolism. JCI Insight *1*.

877 Spagnolo, D.M., Al-Kofahi, Y., Zhu, P., Lezon, T.R., Gough, A., Stern, A.M., Lee, A.V., Ginty, F., Sarachan,
878 B., Taylor, D.L.*, et al.* (2017). Platform for Quantitative Evaluation of Spatial Intratumoral
879 Heterogeneity in Multiplexed Fluorescence Images. Cancer Res *77*, e71-e74.

880 Spencer, S.L., Gaudet, S., Albeck, J.G., Burke, J.M., and Sorger, P.K. (2009). Non-genetic origins of cell-
881 to-cell variability in TRAIL-induced apoptosis. Nature *459*, 428-432.

882 Tan, W.C.C., Nerurkar, S.N., Cai, H.Y., Ng, H.H.M., Wu, D., Wee, Y.T.F., Lim, J.C.T., Yeong, J., and Lim,
883 T.K.H. (2020). Overview of multiplex immunohistochemistry/immunofluorescence techniques in the
884 era of cancer immunotherapy. Cancer Commun (Lond) *40*, 135-153.

885 Thienpont, B., Steinbacher, J., Zhao, H., D'Anna, F., Kuchnio, A., Ploumakis, A., Ghesquière, B., Van
886 Dyck, L., Boeckx, B., Schoonjans, L.*, et al.* (2016). Tumour hypoxia causes DNA hypermethylation by
887 reducing TET activity. Nature *537*, 63-68.

888 Walensky, L.D., and Gavathiotis, E. (2011). BAX unleashed: the biochemical transformation of an
889 inactive cytosolic monomer into a toxic mitochondrial pore. Trends Biochem Sci *36*, 642-652.

890 Yan, Y., Leontovich, A.A., Gerdes, M.J., Desai, K., Dong, J., Sood, A., Santamaria-Pang, A., Mansfield,
891 A.S., Chadwick, C., Zhang, R.*, et al.* (2019). Understanding heterogeneous tumor microenvironment in
892 metastatic melanoma. PLoS One *14*, e0216485.

893

Figure 1

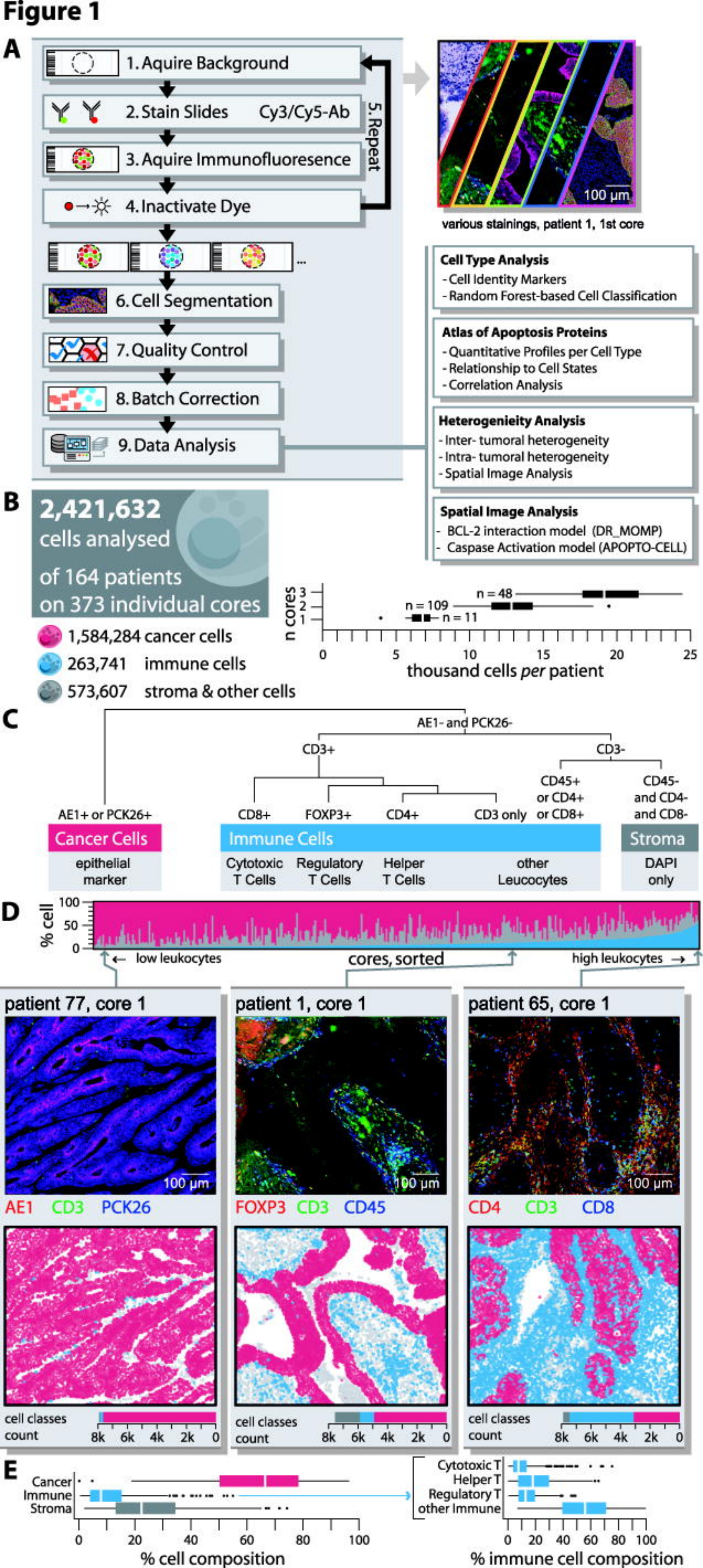
A
1. Aquire Background
2. Stain Slides Cy3/Cy5-Ab
3. Aquire Immunofluoresence
4. Inactivate Dye
5. Repeat
6. Cell Segmentation
7. Quality Control
8. Batch Correction
9. Data Analysis
100 µm
various stainings, patient 1, 1st core
Cell Type Analysis
- Cell Identity Markers
- Random Forest-based Cell Classification
Atlas of Apoptosis Proteins
- Quantitative Profiles per Cell Type
- Relationship to Cell States
- Correlation Analysis
Heterogenieity Analysis
- Inter- tumoral heterogeneity
- Intra- tumoral heterogeneity
- Spatial Image Analysis
Spatial Image Analysis
- BCL-2 interaction model (DR_MOMP)
- Caspase Activation model (APOPTO-CELL)
B
2,421,632
cells analysed
of 164 patients
on 373 individual cores
1,584,284 cancer cells
263,741 immune cells
573,607 stroma & other cells
n cores
n = 48
n = 109
n = 11
thousand cells per patient
C
AE1- and PCK26-
CD3+
CD3-
AE1+ or PCK26+
CD8+
FOXP3+
CD4+
CD3 only
CD45+ or CD4+ or CD8+
CD45- and CD4- and CD8-
Cancer Cells
epithelial marker
Immune Cells
Cytotoxic T Cells
Regulatory T Cells
Helper T Cells
other Leucocytes
Stroma
DAPI only
D
% cell
low leukocytes
cores, sorted
high leukocytes
patient 77, core 1
patient 1, core 1
patient 65, core 1
AE1 CD3 PCK26
FOXP3 CD3 CD45
CD4 CD3 CD8
cell classes count
E
Cancer
Immune
Stroma
% cell composition
Cytotoxic T
Helper T
Regulatory T
other Immune
% immune cell composition

Figure 2

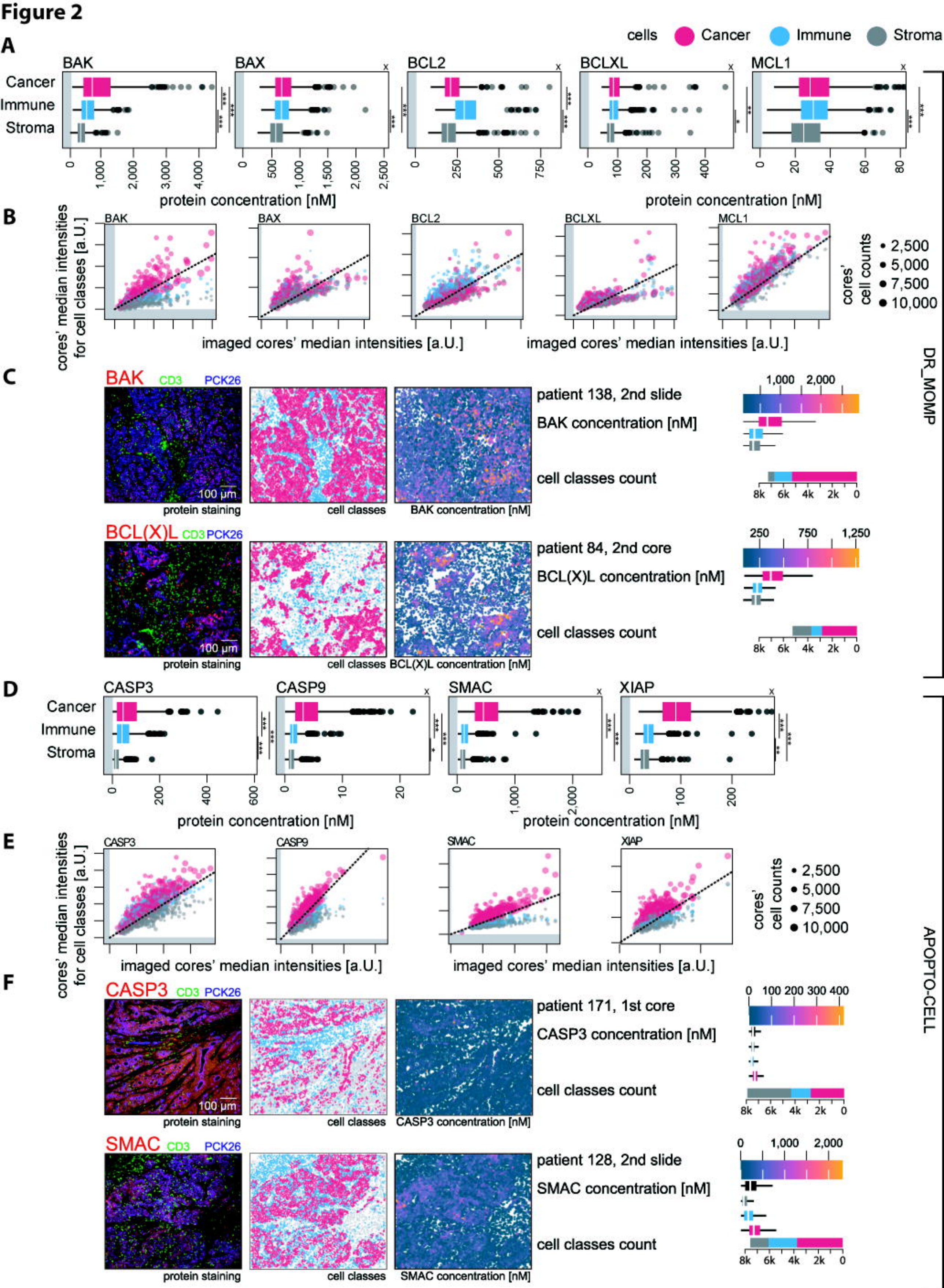
A
cells
Cancer
Immune
Stroma
BAK
BAX
BCL2
BCLXL
MCL1
protein concentration [nM]
B
cores' median intensities for cell classes [a.U.]
imaged cores' median intensities [a.U.]
cores' cell counts
2,500
5,000
7,500
10,000
C
BAK CD3 PCK26
100 µm
protein staining
cell classes
BAK concentration [nM]
patient 138, 2nd slide
BAK concentration [nM]
cell classes count
BCL(X)L CD3 PCK26
BCL(X)L concentration [nM]
patient 84, 2nd core
BCL(X)L concentration [nM]
cell classes count
D
CASP3
CASP9
SMAC
XIAP
E
F
CASP3 CD3 PCK26
CASP3 concentration [nM]
patient 171, 1st core
SMAC CD3 PCK26
SMAC concentration [nM]
patient 128, 2nd slide
DR_MOMP
APOPTO-CELL

Figure 3

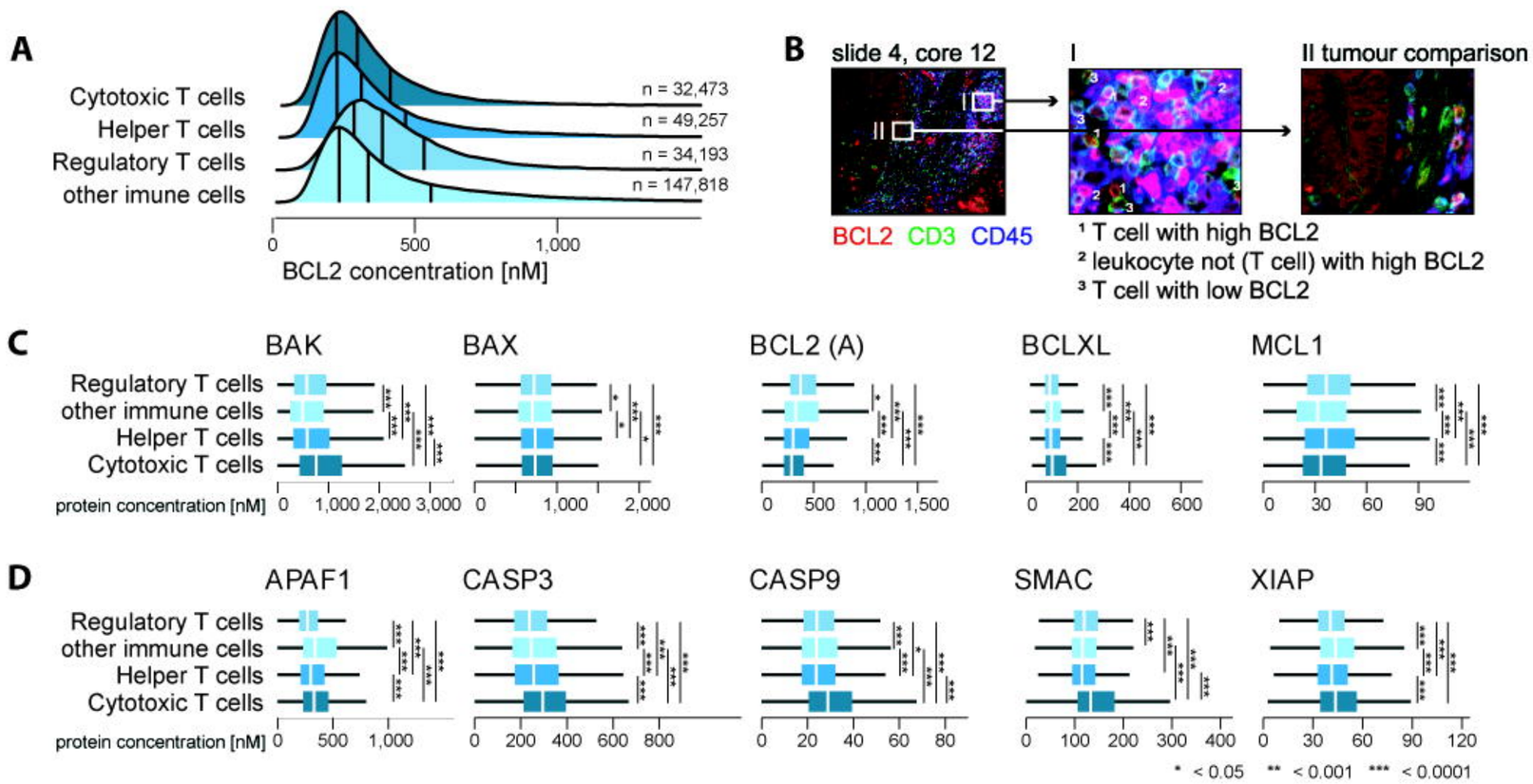
A
Cytotoxic T cells
Helper T cells
Regulatory T cells
other imune cells
n = 32,473
n = 49,257
n = 34,193
n = 147,818
0
500
1,000
BCL2 concentration [nM]
B
slide 4, core 12
I
II tumour comparison
BCL2 CD3 CD45
¹ T cell with high BCL2
² leukocyte not (T cell) with high BCL2
³ T cell with low BCL2
C
BAK
BAX
BCL2 (A)
BCLXL
MCL1
Regulatory T cells
other immune cells
Helper T cells
Cytotoxic T cells
protein concentration [nM]
D
APAF1
CASP3
CASP9
SMAC
XIAP
* < 0.05 ** < 0.001 *** < 0.0001

Figure 4

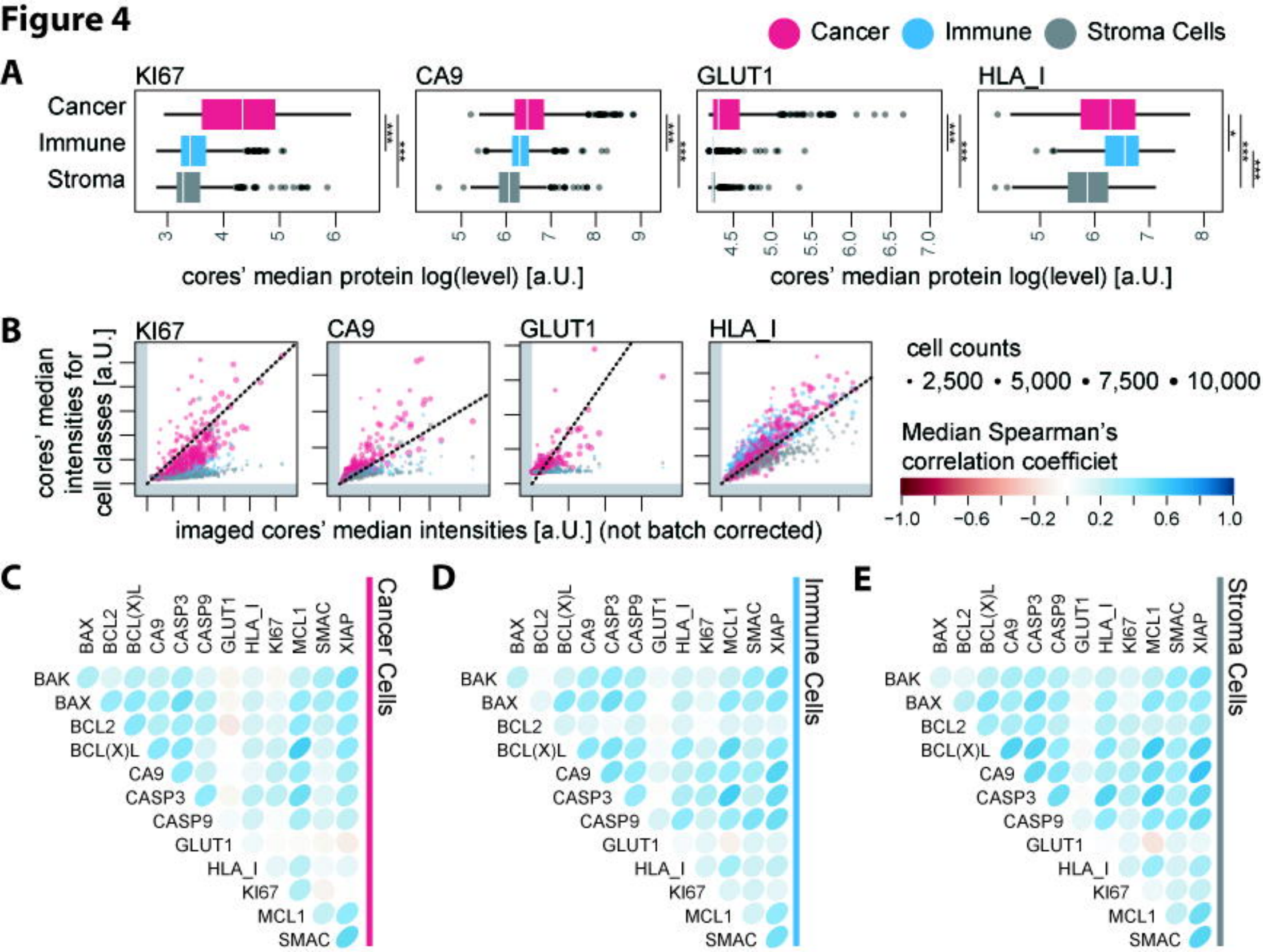
Cancer
Immune
Stroma Cells
A
KI67
CA9
GLUT1
HLA_I
Cancer
Immune
Stroma
cores' median protein log(level) [a.U.]
cores' median protein log(level) [a.U.]
B
KI67
CA9
GLUT1
HLA_I
cores' median intensities for cell classes [a.U.]
imaged cores' median intensities [a.U.] (not batch corrected)
cell counts
• 2,500 • 5,000 • 7,500 • 10,000
Median Spearman's correlation coefficiet
−1.0 −0.6 −0.2 0.2 0.6 1.0
C
Cancer Cells
D
Immune Cells
E
Stroma Cells
BAK
BAX
BCL2
BCL(X)L
CA9
CASP3
CASP9
GLUT1
HLA_I
KI67
MCL1
SMAC
XIAP

Figure 5

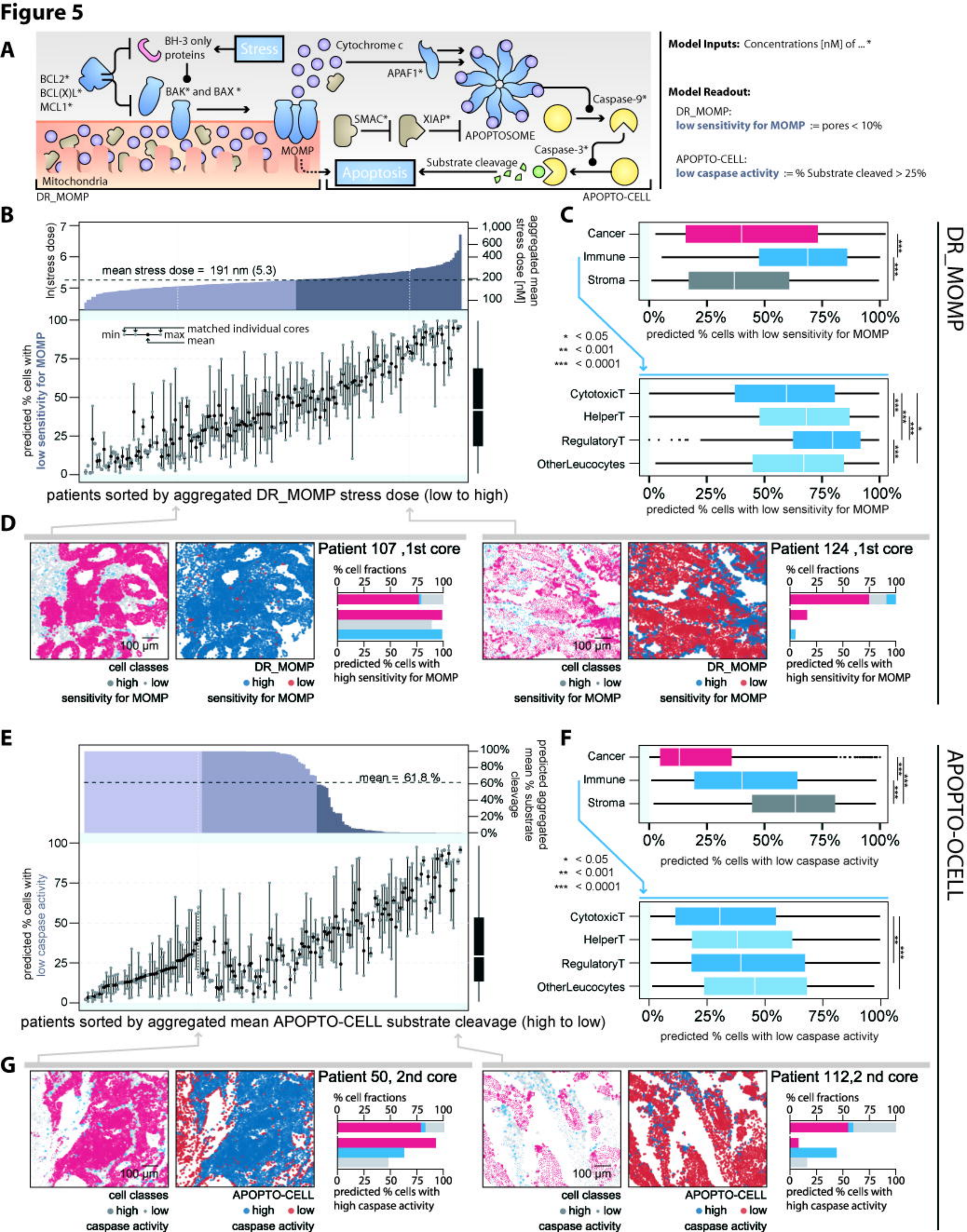
A
BH-3 only proteins
Stress
Cytochrome c
BCL2*
BCL(X)L*
MCL1*
BAK* and BAX *
APAF1*
Caspase-9*
SMAC*
XIAP*
APOPTOSOME
MOMP
Caspase-3*
Substrate cleavage
Apoptosis
Mitochondria
DR_MOMP
APOPTO-CELL
Model Inputs: Concentrations [nM] of ... *
Model Readout:
DR_MOMP:
low sensitivity for MOMP := pores < 10%
APOPTO-CELL:
low caspase activity := % Substrate cleaved > 25%
B
ln(stress dose)
mean stress dose = 191 nm (5.3)
aggregated mean stress dose [nM]
predicted % cells with low sensitivity for MOMP
min
max
matched individual cores
mean
patients sorted by aggregated DR_MOMP stress dose (low to high)
C
Cancer
Immune
Stroma
predicted % cells with low sensitivity for MOMP
* < 0.05
** < 0.001
*** < 0.0001
CytotoxicT
HelperT
RegulatoryT
OtherLeucocytes
DR_MOMP
D
Patient 107 ,1st core
Patient 124 ,1st core
100 µm
cell classes
high low
sensitivity for MOMP
DR_MOMP
high low
sensitivity for MOMP
% cell fractions
predicted % cells with high sensitivity for MOMP
E
mean = 61.8 %
predicted aggregated mean % substrate cleavage
predicted % cells with low caspase activity
patients sorted by aggregated mean APOPTO-CELL substrate cleavage (high to low)
F
predicted % cells with low caspase activity
APOPTO-CELL
G
Patient 50, 2nd core
Patient 112,2 nd core
cell classes
high low
caspase activity
APOPTO-CELL
high low
caspase activity
% cell fractions
predicted % cells with high caspase activity

Figure 6

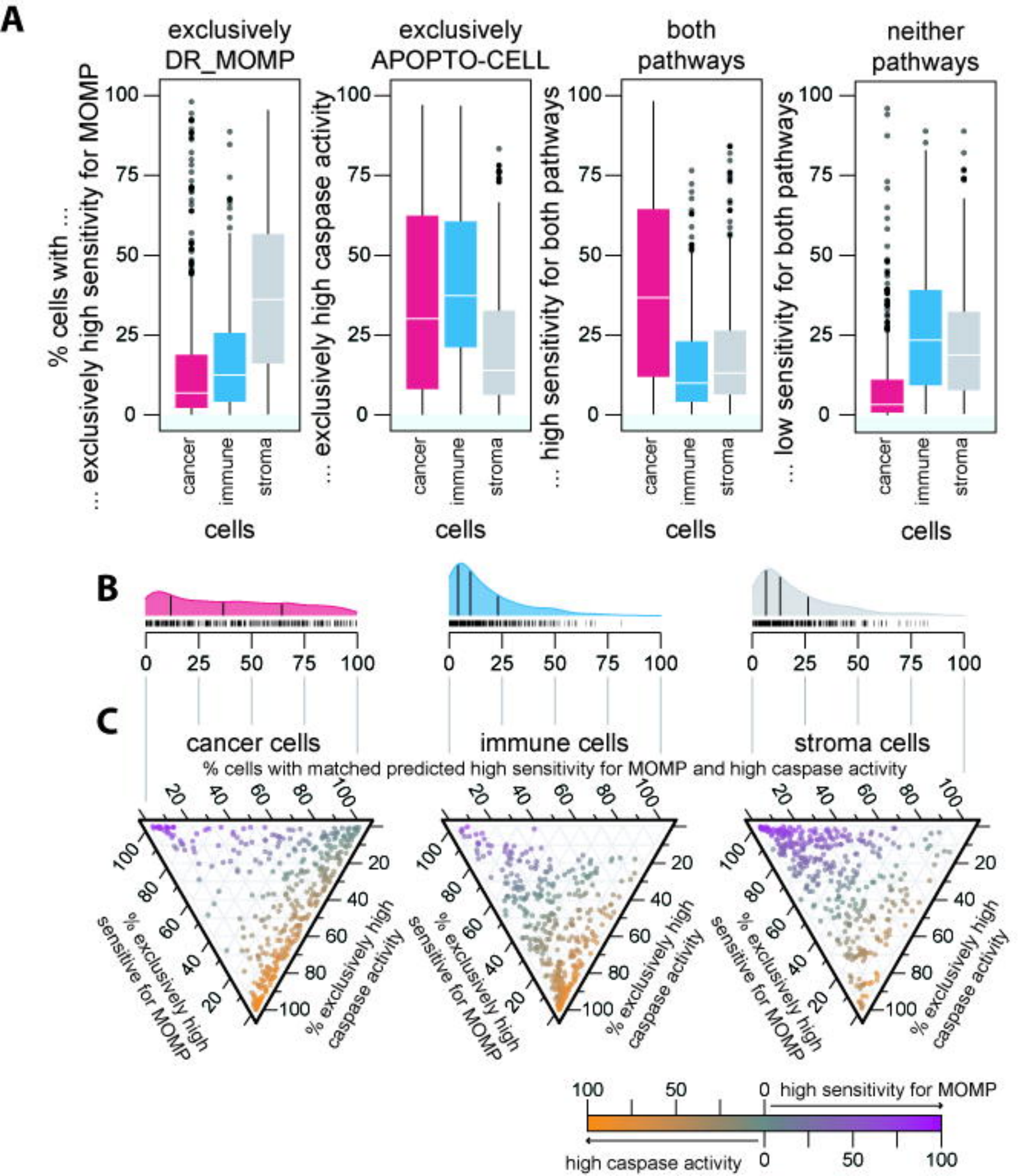
A
exclusively DR_MOMP
exclusively APOPTO-CELL
both pathways
neither pathways
% cells with ...
... exclusively high sensitivity for MOMP
... exclusively high caspase activity
... high sensitivity for both pathways
... low sensitivity for both pathways
100
75
50
25
0
cancer
immune
stroma
cells
B
0
25
50
75
100
C
cancer cells
immune cells
stroma cells
% cells with matched predicted high sensitivity for MOMP and high caspase activity
20
40
60
80
100
% exclusively high sensitive for MOMP
% exclusively high caspase activity
100
50
0
high sensitivity for MOMP
high caspase activity
0
50
100

Figure 7

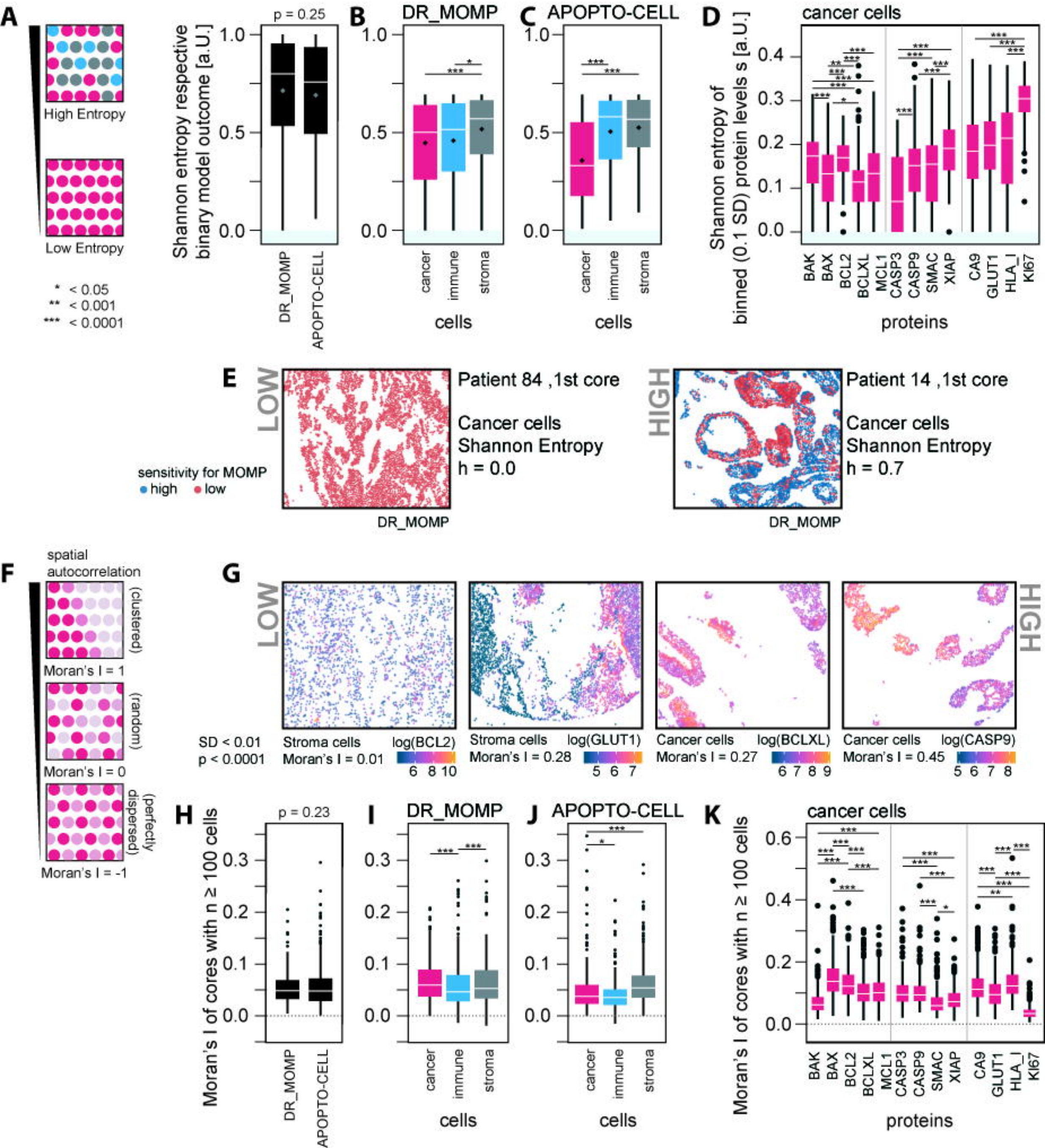
A
High Entropy
Low Entropy
* < 0.05
** < 0.001
*** < 0.0001
p = 0.25
Shannon entropy respective binary model outcome [a.U.]
DR_MOMP
APOPTO-CELL
B
DR_MOMP
C
APOPTO-CELL
cancer
immune
stroma
cells
D
cancer cells
Shannon entropy of binned (0.1 SD) protein levels s [a.U.]
BAK
BAX
BCL2
BCLXL
MCL1
CASP3
CASP9
SMAC
XIAP
CA9
GLUT1
HLA_I
KI67
proteins
E
LOW
HIGH
sensitivity for MOMP
high
low
Patient 84 ,1st core
Cancer cells
Shannon Entropy
h = 0.0
Patient 14 ,1st core
Cancer cells
Shannon Entropy
h = 0.7
DR_MOMP
F
spatial autocorrelation
(clustered)
Moran's I = 1
(random)
Moran's I = 0
(perfectly dispersed)
Moran's I = -1
G
LOW
HIGH
SD < 0.01
p < 0.0001
Stroma cells
log(BCL2)
Moran's I = 0.01
6 8 10
Stroma cells
log(GLUT1)
Moran's I = 0.28
5 6 7
Cancer cells
log(BCLXL)
Moran's I = 0.27
6 7 8 9
Cancer cells
log(CASP9)
Moran's I = 0.45
5 6 7 8
H
p = 0.23
Moran's I of cores with n ≥ 100 cells
DR_MOMP
APOPTO-CELL
I
DR_MOMP
J
APOPTO-CELL
cancer
immune
stroma
cells
K
cancer cells
Moran's I of cores with n ≥ 100 cells
BAK
BAX
BCL2
BCLXL
MCL1
CASP3
CASP9
SMAC
XIAP
CA9
GLUT1
HLA_I
KI67
proteins